Ocean Modelling 36 (2011) 179–197

Contents lists available at ScienceDirect

Ocean Modelling

journal homepage: www.elsevier.com/locate/ocemod

Enhanced estimation of sonobuoy trajectories by velocity reconstruction with near-surface drifters

Y. Chang [a], D. Hammond [b], A.C. Haza [a], P. Hogan [c], H.S. Huntley [d], A.D. Kirwan Jr. [d], B.L. Lipphardt Jr. [d], V. Taillandier [e], A. Griffa [a,f], T.M. Özgökmen [a,*]

[a] RSMAS/MPO, University of Miami, Miami, FL 33149, USA
[b] Advanced Avionics, Inc., 607 Louis Dr., Warminster, PA 18974, USA
[c] Naval Research Laboratory, Stennis Space Center, MS 39529, USA
[d] School of Marine Science & Policy, University of Delaware, Newark, DE 19716, USA
[e] Laboratoire Océanologique of Villefranche, CNRS, France
[f] ISMAR-CNR, La Spezia, Italy

ARTICLE INFO

Article history:
Received 5 April 2010
Received in revised form 17 November 2010
Accepted 21 November 2010
Available online 30 November 2010

Keywords:
Lagrangian data assimilation
Predictability
Drifter trajectories

ABSTRACT

An investigation to improve trajectory prediction using Lagrangian data is presented. The velocity field of a data assimilating model, EAS-16, is corrected using drifter observations taken during an experiment off Taiwan. The results are tested using another independent Lagrangian data set provided by sonobuoys launched in the same area. The latter have instrument chains that extend well into the water column. Consequently the corrected model velocities were projected into the water column in order to calculate sonobuoy trajectories. The drifter and sonobuoy trajectories both show two distinct regimes in the considered area of approximately 1/2° square. One regime is dominated by shelf dynamics, the other by meandering of the Kuroshio, with a sharp boundary dividing the two. These two regimes are not reproduced by the trajectories of the EAS-16 model. When the drifter data are blended with the model velocities, synthetic sonobuoy trajectories track the observed ones much better, and the two regimes are clearly depicted. Two different methods for the velocity reconstruction are tested. One is based on a variational approach and the other on a normal mode decomposition. Both methods show qualitatively similar improvements in the prediction of sonobuoys trajectories, with a quantitative improvement in the total rms error of approximately 50% and 25%, respectively.

1. Introduction

Operational forecasting systems are based on two complementary components, a monitoring system and an ocean modeling system. The model ocean state is routinely corrected using the data from the monitoring system, and forecasts are provided running the model forward starting from a corrected (constrained) initial state. Forecast skills have dramatically increased in the last years, but their main limiting factor may well be related to the density and quality of the observations that are used to constrain the analysis and re-initialize the model.

For many applications, there is now a significant demand for Lagrangian products from operational models. Examples are search and rescue, drifting sensor arrays, and mitigation in case of pollutants, such as oil spills. Lagrangian predictability, i.e. prediction of particle motion, is especially demanding for a number of reasons. Particle trajectories are obtained by integrating the velocity, so that even small errors in the forecasts of Eulerian velocity tend to accumulate and grow (Griffa et al., 2004). Also, particle motion is often inherently chaotic, namely it exhibits a high dependence on initial conditions even in very simple flows (Aref, 1984). Thus, even a slight difference in initial conditions in space and time can result in significantly different behaviors. A natural avenue to improve trajectory prediction appears to be the assimilation of Lagrangian data that provide direct trajectory information.

In the last decade, a number of schemes for using Lagrangian data for forecasting have been proposed. Lagrangian instruments are floating devices (acting as proxies for fluid particles) that provide information on their positions and possibly on other environmental parameters at discrete time intervals. Velocity information can be obtained from consecutive position observations, provided that the time interval is smaller than the typical Lagrangian time scale T_L, namely the time over which particle velocity is self-correlated.

* Corresponding author.
E-mail addresses: ychang@rsmas.miami.edu (Y. Chang), david.s.hammond@earthlink.net (D. Hammond), ahaza@rsmas.miami.edu (A.C. Haza), patrick.hogan@nrlssc.navy.mil (P. Hogan), helgah@UDel.Edu (H.S. Huntley), adk@udel.edu (A.D. Kirwan Jr.), brucel@UDel.Edu (B.L. Lipphardt Jr.), taillandier@obs-vlfr.fr (V. Taillandier), agriffa@rsmas.miami.edu (A. Griffa), tozgokmen@rsmas.miami.edu (T.M. Özgökmen).

1463-5003/$ - see front matter © 2010 Elsevier Ltd. All rights reserved.
doi:10.1016/j.ocemod.2010.11.002

For the surface ocean, T_L typically varies in the range of 1–5 days (Bauer et al., 2002; LaCasce, 2008). Various methods have been suggested for both velocity reconstruction (Toner et al., 2001; Taillandier et al., 2006a) and actual assimilation (Molcard et al., 2003; Taillandier et al., 2006b; Kuznetsov et al., 2003). The former consists of improving the velocity field from off-line circulation model output by blending it with the Lagrangian data, while assimilation implies that the circulation model itself is corrected (often by sequential re-initialization) using the corrected velocity fields and adequately balanced mass fields. Reconstruction can be seen as a first step toward assimilation, but it is also valuable per se, especially for operational purposes, since it is extremely flexible and can be applied to the output of any model used in case of an accident or emergency, even when the model does not have a full assimilation capability.

Two main approaches have been followed for the reconstruction and assimilation of Lagrangian data. The first approach is based on estimating velocities along trajectories as the ratio between observed position differences and time increments (e.g., Hernandez et al., 1995) and directly using these velocities to correct the model results. The second approach introduces an observational operator based on the particle advection equation and corrects the Eulerian velocity field by requiring the minimization of the difference between observed and modeled trajectories (e.g., Molcard et al., 2003). These approaches have been implemented using several methodologies, including optimal interpolation (OI; Molcard et al., 2003; Özgökmen et al., 2003; Molcard et al., 2005), mode decomposition techniques (Toner et al., 2001), Kalman filtering (Ide et al., 2002; Kuznetsov et al., 2003; Salman et al., 2006), variational methods (Kamachi and O'Brien, 1995; Taillandier et al., 2006a; Taillandier and Griffa, 2006; Nodet, 2006), and particle filter methods (Salman, 2008b,a; Krause and Restrepo, 2009). Apte et al. (2008) have developed a Markov-chain Monte Carlo sampling strategy for Lagrangian data assimilation that eliminates problems with the Kalman filter approach near saddle points in the flow field. Such Bayesian methods should play an increasingly important role in assimilating and blending Lagrangian and Eulerian data.

While these methods have been thoroughly tested using synthetic data in the framework of numerical models, application to in situ data and actual operational testing are just beginning. The variational method of Taillandier et al. (2006a) has been applied to Argo float data assimilation in the northwestern Mediterranean Sea (Taillandier et al., 2006b, 2010) and to drifter data reconstruction in the Adriatic Sea (Taillandier et al., 2008). An application of the mode-decomposition method to 50 m drogued drifters and a primitive equation model of the Gulf of Mexico has been reported in Toner et al. (2001). These studies show significant and consistent changes in the ocean circulation and in the Lagrangian pathways, but a full and quantitative evaluation of the approaches using independent data is still lacking. This study provides the first such assessment.

Here, we address this issue with a unique data set collected from an exercise off Taiwan in October 2007. The data are composed of 30 SVP (Surface Velocity Program) drifters and 28 sonobuoys with instrumented chains deployed in a small grid (approximately 1/2° square) over three days during a Littoral Warfare Advanced Development experiment (LWAD07). The SVP drifters are carefully designed to follow the flow field at approximately 15 m, while the sonobuoys respond to the flow along the entire length of the instrument chain. In addition to this data, hindcasts for the experiment are provided from a data assimilating model, the Naval Research Laboratory East Asian Seas 1/16° ocean model (EAS-16). In the present investigation, the velocity field is reconstructed using two different methods that blend the output of EAS-16 with the data from the SVP drifters and statistically project the velocity correction over the water column. The corrected velocity fields are then independently tested using the sonobuoy data. Synthetic sonobuoy trajectories are computed using an appropriate drag model applied to the corrected velocities, and they are quantitatively compared with the observed sonobuoy trajectories. The dense array of Lagrangian data from drifting sensors that respond to currents at different depths and the near-operational high resolution data assimilating model provide an opportunity to evaluate Lagrangian predictability.

Our investigation has a number of unique and novel aspects. It provides an example of a truly operational application, targeted to predict the motion of sonobuoys within the framework of an LWAD exercise. The region of application is interesting and challenging, since it is located along the shelf break at the boundary of the Kuroshio, encompassing two distinct flow regimes in a relatively small area, divided by a geostrophic front. Predicting the exact location of the front at such scales is challenging for a numerical model. Also, the use of two different methods of reconstruction provides an interesting opportunity to evaluate the utility of Lagrangian data blending with different approaches. Finally and most importantly, the present application provides a first example of independent testing of the results, since *the reconstruction is based on drifter data only*, while *the testing is performed using the sonobuoy trajectories*. Sonobuoys not only respond differently to currents than drifters do, but they also have been launched at slightly different times (order of one day difference) from the drifters, which is significant for Lagrangian applications characterized by time scales of 1–2 days. Positive results in the case of sonobuoy trajectory prediction are expected to be meaningful also for other applications that involve forecasts of floating quantities in the upper ocean. Potential applications include prediction of the pathways of pollutants or invasive species such as jelly fish.

The paper is organized as follows. The LWAD07 experiment and the data sources are described in Section 2. In Section 3, the two methods used to blend the Lagrangian data with EAS-16 are discussed and their results are shown. (More details on the methods are provided in the Appendices.) The assessment of the reconstructed velocities using sonobuoy data is given in Section 4. We conclude with a summary of our findings and a discussion of the role of Lagrangian data in enhancing Lagrangian forecasts.

2. Data sources

2.1. LWAD07: SVP drifters

The data set we are using for the reconstruction consists of 30 SVP drifters, whose configuration followed the standards of the Global Drifter Program. The drifter's drogue is centered at 15 m beneath the surface, thus ensuring that the drifters capture near-surface velocities. Determining drogue loss remains challenging, even when submergence measurements are provided, as in this case. Using the standard procedure of equating a sharp drop in the submergence indicator with drogue loss, only one of the drifters lost its drogue during the analysis period. We have chosen to include its full data record nonetheless, since its statistics and behavior are indistinguishable from the others'.

The drifters were launched during the window of October 8–12, 2007 UTC in the East China Sea. The deployment area straddles the edge of the continental shelf and is thus near the Kuroshio, a strong western boundary current. The shelf dynamics are dominated by the tides. An overview of the geographical and topographical context of the launch area is given in Fig. 1, along with a sample model velocity field. All but one of the drifters reported continuously for at least the first two weeks, and most of them up to 25 days, the exception being a drifter that died after just one day in the water. GPS positions and sea surface temperatures were recorded at

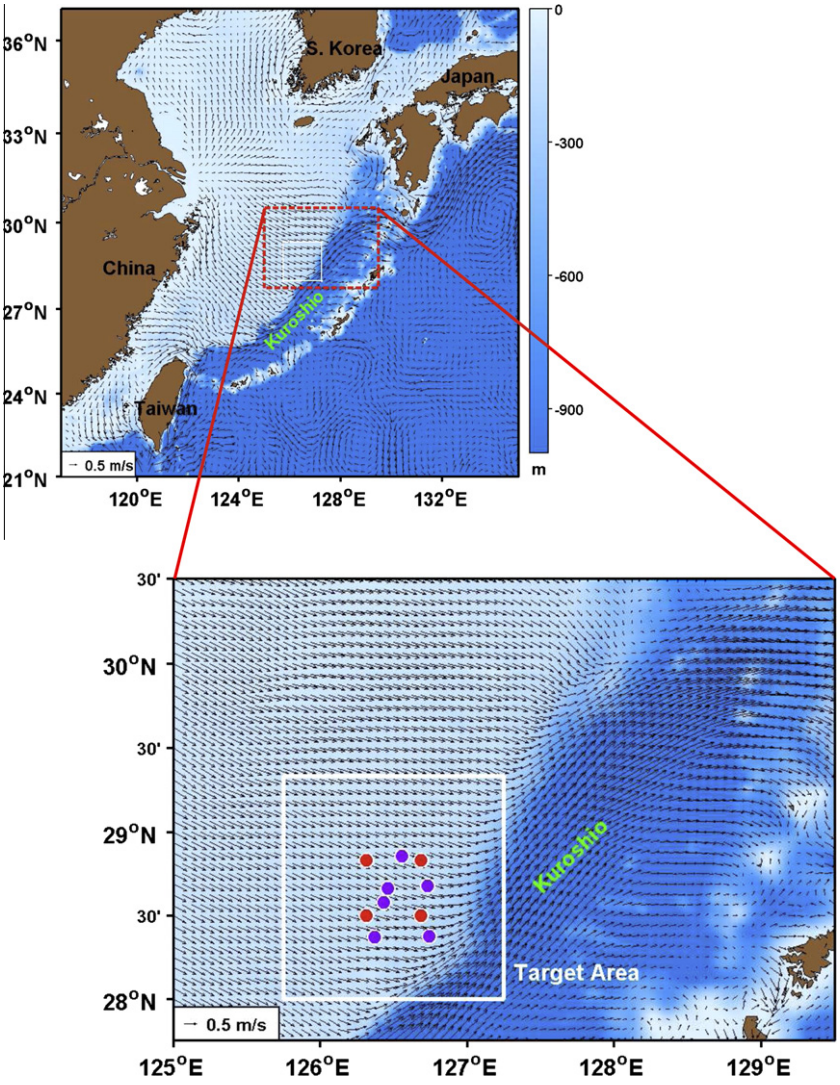

Fig. 1. Overview of drifter launch locations. Purple disks indicate launches performed en route to the standard stations, while red disks indicate the four standard stations. Bottom topography is displayed in the color field to illustrate the shelf edge. The velocity field is a typical EAS-16 model field. (For interpretation of the references to colour in this figure legend, the reader is referred to the web version of this article.)

approximately fifteen minute intervals. In a preprocessing step, duplicate entries and those implying unrealistically large velocities or accelerations were deleted from the records.

Details on the launch times and on time coverage during the first few days of the experiment, that are the main focus of the present application, are shown in Fig. 2(a). The first six drifters were launched around 22:00 October 8, while the ship was en route (purple dots in Fig. 1), while the other drifters were deployed in six successive deployments of four instruments each, reusing four standard launch locations each time (red dots in Fig. 1). The six successive deployments roughly correspond to 22:00 October 9, 4:00 October 10, 15:00 October 10, 4:00 October 11, 16:00 October 11, and 4:00 October 12. Each event of four launches spans approximately 1.5 h, except for one event which includes a launch 4 h prior to the rest. Also, one event had two southwest launches but none from the northwest corner.

The drifter trajectories corresponding to the first two days of the experiment (October 8–10, 2007) are shown in Fig. 3(a). The motion of the drifters can be categorized by the region of the test site in which they were deployed, and it shows the presence of two very distinct regimes. Drifters deployed in the northwestern

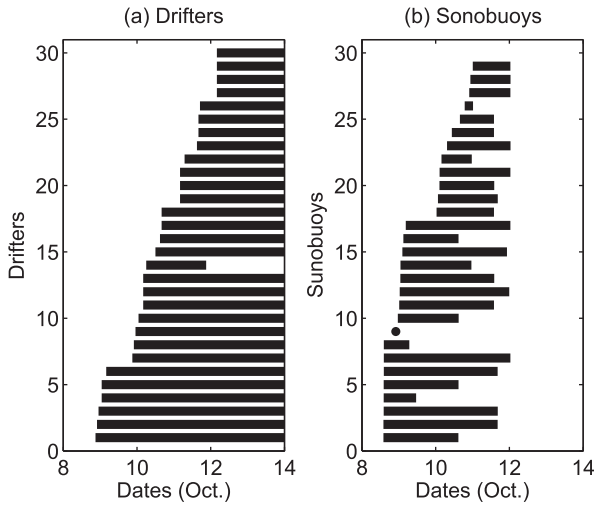

Fig. 2. Time spans of (a) drifters and (b) sonobuoys over the period October 8–14, 2007.

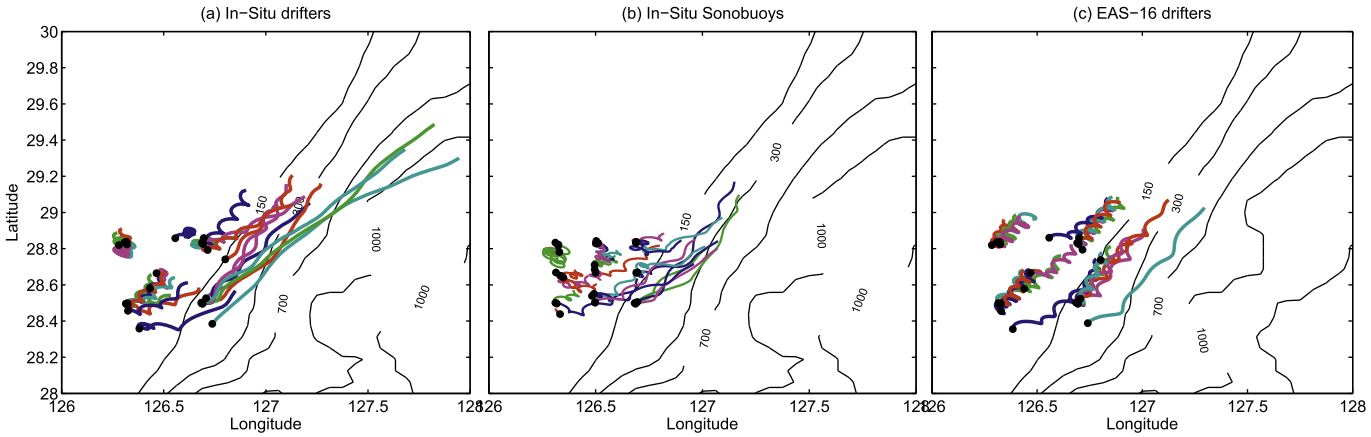

Fig. 3. (a) Observed drifter trajectories, (b) observed sonobuoy trajectories, and (c) modeled drifter trajectories using EAS-16, during the first two days of the experiment, October 8–10 2007. Colors depict trajectories of corresponding drifters in panels (a) and (c). Black circles mark initial locations.

corner, characterized by shallower water and shelf dynamics, show a looping pattern with almost no net drift. The semi-diurnal period of the looping is indicative of tidal forcing. The drift of instruments deployed in the southeastern corner of the test site is influenced by the Kuroshio as characterized by rapid advection to the northeast with little tidal fluctuation. Drifters deployed in the transition zone between the two corners exhibit characteristics of both the southeastern and northwestern corner deployments. These drifters generally start slowly looping to the east or northeast. Some of them are pulled closer into the influence of the Kuroshio, and then eventually they get swept up into the Kuroshio and move rapidly to the northeast.

2.2. LWAD07: CDMR sonobuoys

In addition to the SVP drifters, 28 Compact Deployable Multistatic Receiver (CDMR) sonobuoys were deployed during the LWAD07 experiment from October 8–11, 2007 in the same target area as the SVP drifters. The CDMR are experimental Navy sonobuoys similar in physical characteristics to the AN/SSQ-101 ADAR sonobuoy (Fig. 4). They consist of an inflatable toroid shaped surface float with an approximate diameter of 0.45 m, a length of cable and bungee, two cylindrical cable packs, and a large horizontal planar hydrophone array (diameter about 6 m) set to a maximum depth of 27.4 m. Each sonobuoy communicated its position to a logging station via an Iridium satellite link.

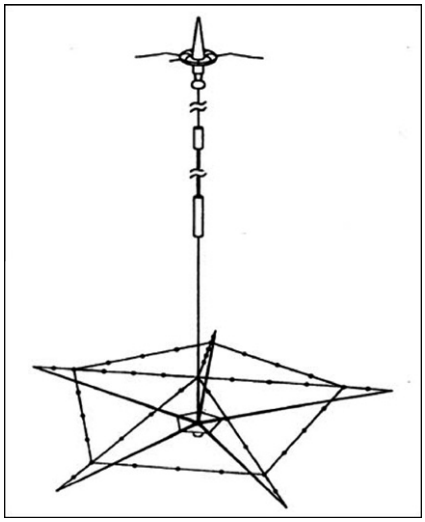

Fig. 4. Diagram of a sonobuoy.

The launch times and life spans of the sonobuoys are summarized in Fig. 2(b). The average operating life span of the deployed CDMR during this exercise was 43 h with a maximum of 82 h. The first deployment of eight sonobuoys occurred around 14:00 October 8, i.e. approximately 7 h before the first drifter deployment. Subsequent deployments span the period from 22:00 October 8 to 0:00 October 11. Some of the sonobuoys were launched simultaneously with drifter deployments, but in many cases there is no direct correspondence between sonobuoy and drifter launch times. Moreover, launch locations are slightly different.

Sonobuoy trajectories are shown in Fig. 3(b) during the same time interval as the drifters in Fig. 3(a). The sonobuoy trajectories show a similar general pattern as the drifters, characterized by the two flow regimes, but they also show significant differences. Sonobuoys launched in the northwestern area show a more pronounced southward drift than the drifters, and those entrained in the Kuroshio experience a somewhat slower drift. The differences are likely due to two main factors: (a) the different response of sonobuoys to currents at different depths and (b) the differences in launch times and locations. Given the high variability of the flow and the inherent chaotic nature of Lagrangian motion, even slight differences in the initial conditions can lead to significantly different trajectories.

2.3. The EAS-16 system

The Naval Research Laboratory East Asian Sea 1/16° ocean model (EAS-16) is exercised daily using atmospheric forcing provided by the Navy Operational Global Atmospheric Prediction System (NOGAPS). It is an adaptation of the operational Navy Coastal Ocean Model (NCOM; Martin, 2000) and takes its boundary forcing from a global 1/8° NCOM implementation. These are primitive equation models, with hydrostatic, Boussinesq, and 3D-incompressibility approximations. 41 mixed-coordinate layers are used, with σ coordinates from the surface down to the shelf break around 137 m depth and z levels below. For our analysis, the output has been interpolated to constant depths at 1, 2, 5, 10, 20, 40, 60, 80, 100, and 150 m. Eight tidal components (K1, O1, P1, Q1, K2, M2, N2, and S2) are incorporated through tidal potential forcing from NCOM. The model assimilates sea surface height anomaly and temperature through the Modular Ocean Data Assimilation System (MODAS; Fox et al., 2002). For a more detailed description of the model and a discussion of the Eulerian validations carried out, see Riedlinger et al. (2006).

While EAS-16 is employed here mainly because it was the operational model accompanying the LWAD07 experiment, it needs to be stated that EAS-16 is not what the Navy considers to be the

state-of-the-art forecasting system anymore. Models with 1 km and 3 km horizontal resolutions and other data assimilations systems have been used in the LWAD experiment conducted in 2009. Results from this more recent application will be reported in a future study.

Examples of drifter trajectories computed using the EAS-16 output are shown in Fig. 3(c) for the same period as for the in situ drifters (Fig. 3(a)). The simulated trajectories are initialized at the launch locations of the observed drifters and are computed using a 4th order Runge–Kutta method. Compared with Fig. 3(a), the EAS-16 trajectories show a more homogeneous drift toward the northeast and a more pronounced looping throughout the area, without indicating any significant difference between the two regimes, on the shelf and within the Kuroshio. This suggests that the details of the Kuroshio meandering are not correctly reproduced in the model, which is not surprising given the high nonlinearity of the region and the small size of the target domain relative to the resolution of the model and of the assimilation observing system.

3. Blending Lagrangian drifters and EAS-16 output

In order to improve upon the Lagrangian prediction results of EAS-16 cited above, we employ a tool that has proven useful for extending Eulerian predictability horizons, namely data assimilation. Since we are primarily interested in Lagrangian forecasts, it is natural to consider Lagrangian observations and how best to blend them with the model output. As discussed in the Introduction, correcting off-line velocities is different from performing full assimilation including balancing of the mass variables and re-initialization of the model. On the other hand, the procedure can be seen as a first step toward assimilation, and it has the advantage of being flexible, portable, and easy to implement.

The reconstruction of the velocity field using drifter data and EAS-16 output is performed using two methods based on different approaches. One method, Lagrangian variational analysis (LAVA), is based on the variational approach put forward by Taillandier et al. (2006a), where model velocities are corrected by minimizing the distance between observed and modeled drifter positions. The other method, Normal Mode Analysis (NMA), is based on estimating velocities along trajectories and optimally blending them with model velocities (Toner et al., 2001). For both methods, a two step strategy is adopted. First, the drifter data are used to correct the EAS-16 velocity at a 10-m depth, approximately corresponding to the drogue nominal depth of 15 m. The velocity correction is then projected into the water column by using covariance methods developed from the original unblended EAS-16 output. Starting with the 20-m model level instead makes little difference, as there is little vertical shear at these depths in the model. Without data blending, the rms separation distances between observed and model trajectories at 10 m and at 20 m after 24 h differ by less than 0.05% or about 7 m.

3.1. Lagrangian variational analysis (LAVA)

The LAVA approach (Taillandier et al., 2006a) has been previously applied to Argo float data assimilation in the northwestern Mediterranean Sea (Taillandier et al., 2006b, 2010) and to drifter data reconstruction in the Adriatic Sea (Taillandier et al., 2008). Some details of the method are given in Appendix A, while the specific configuration used here is discussed below.

The method has been applied on an extensive domain, encompassing 123°–129° E and 26°–32° N, so that the drifter initial locations are centered in the computational domain and their evolution during the experiment is captured. Even though the specific application in this paper is limited to smaller space scales and short time scales of 1 or 2 days, the method has actually been applied to a longer period, extending 25 days from October 8 until November 2, 2007, in order to check the variability of the process. A total of 27 of the 30 deployed drifters have been used in the reconstruction, since the other three do not last through the whole analysis period.

The input data for the reconstruction are the two-dimensional velocity fields from the 10-m level of EAS-16 for the 25 days with $\Delta t = 1$ h, and the positions of the 27 drifters. In order to minimize the errors that may be caused by the time difference between the two input data sets, the drifter positions are interpolated to the time steps of the velocity fields. The three-dimensional EAS-16 data set is then used to statistically project the corrected velocity down to the 150 m depth, corresponding to the ten vertical analysis levels of the model.

The basic concept of LAVA consists of correcting the model velocity by minimizing the difference between the observed drifter positions and the model forecasted positions from numerical trajectories (see Appendix A). The local correction along the drifter path, $\Delta\mathbf{u}$, is assumed to be characterized by some basic correlation scales in time (T) and space (R), characterizing the persistence of the flow. $\Delta\mathbf{u}$ is extended with scale R along the path and is assumed to be constant in time over T, where T must be smaller than or of the same order as the Eulerian time scale T_E. The correction is performed over sequences with steps $\tau \leqslant T$, that are also required to be no longer than the Lagrangian time scale T_L (Molcard et al., 2003).

These main scales have been identified by computing Eulerian and Lagrangian autocovariances in a preliminary analysis of the drifter data and the model velocity timeseries. As discussed in Section 2, the region of interest is characterized by two very different regimes. The shelf region is shallow and dominated by weak currents, while the deep area is dominated by the presence of the Kuroshio with strong and highly correlated currents. Despite these differences, the time scales appear relatively homogeneous in the domain with dominant mesoscale Eulerian time scales T_E on the order of 1 week, while the Lagrangian time scale $T_L \approx 1$–2 days, which is typical for the upper ocean. In addition to the mesoscale, there is also a strong tidal signal with a period of 12 h. In the present application, as in previous work (Taillandier et al., 2006a, 2008), we focus on corrections at the mesoscale, since higher frequency corrections would require an unrealistically high data coverage. To this end, the correction is computed considering the 12-h low-pass filtered velocity field. A number of preliminary tests have been performed considering various parameter values for T and τ, and the results appear to be quite robust. The results reported in the following are obtained for $\tau = 6$ h and 3 h for the deep and shallow areas, respectively. T is chosen to equal τ, ($T = \tau$), which implies that the procedure is applied over sequences of 1 step only.

As for the space scales, we expect that the differences between the two regimes will be more significant and that they are separated by well defined frontal dynamics. Analysis of the EAS-16 velocity field suggests that the 300 m isobath approximates the boundary between the two regimes (Fig. 5(a)). We select two different space scales, 20 km for the deep region and 10 km for the shallow one (cf. Taillandier et al., 2008). Notice that since the spatial correlation structure is modeled as the solution of a diffusion equation (Derber and Rosati, 1989; Weaver and Courtier, 2001), anisotropic correlations can be taken into account, which are expected to occur for strongly sheared currents flowing along topography.

Fig. 5 gives an example of the velocity field in the area covered by the drifters. Panel (a) shows the original EAS-16 field, panel (b) the corrected field, and panel (c) the difference field. The correction

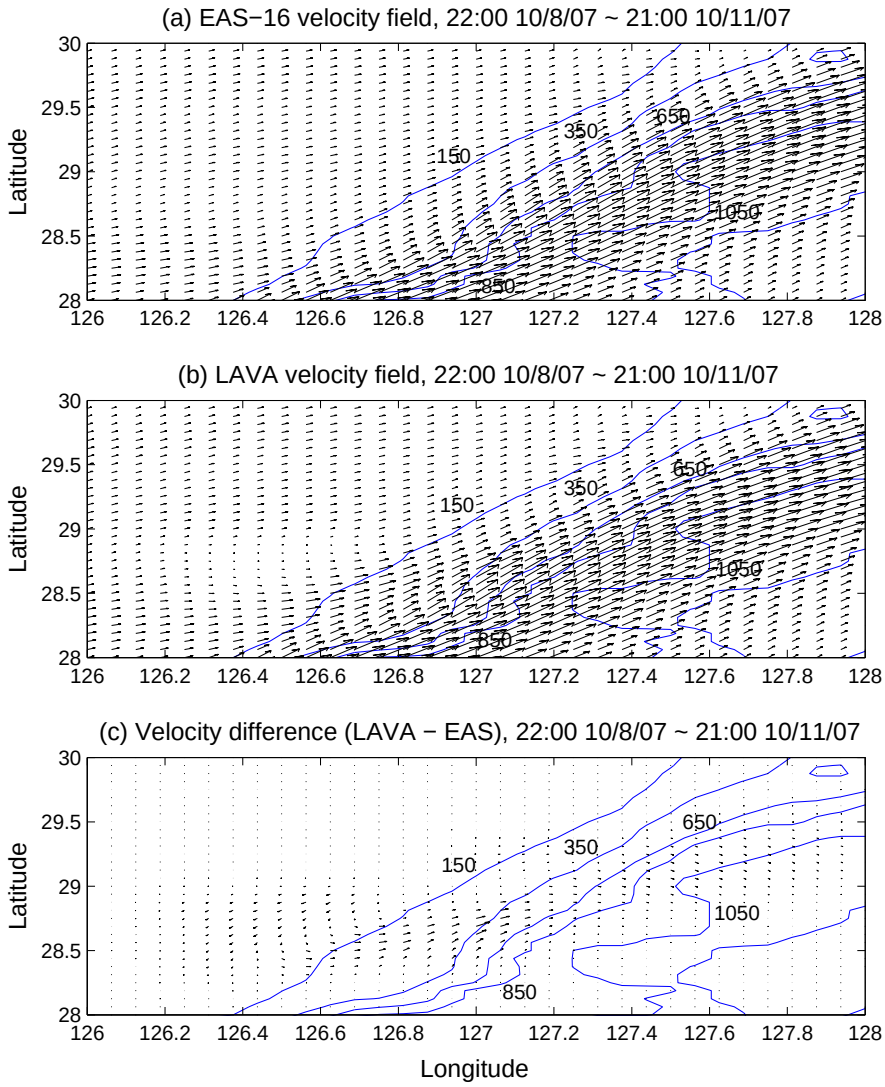

Fig. 5. Velocity vectors that show flow patterns in the region. The velocities are averaged over 3 days from 22:00 October 8 through 21:00 October 11, 2007. (a) Original EAS-16 velocity; (b) corrected LAVA velocity; (c) velocity difference (LAVA − EAS-16). Blue lines indicate isobaths, with labels in m. (For interpretation of the references to colour in this figure legend, the reader is referred to the web version of this article.)

induced by the drifters tends to decrease the velocity in the shelf area, while it increases it in the Kuroshio and in the transition area.

Once we have computed the estimated velocity field at the drifter level, we need to calculate its vertical projections in order to estimate the velocities at other depths. To do this, the vertical correlation function, C, can be calculated for the two velocity components separately as

$$C_{z_o}(x,y,z) = \frac{\langle u'(x,y,z_o,t)u'(x,y,z,t)\rangle}{\langle u'(x,y,z_o,t)u'(x,y,z_o,t)\rangle}, \tag{1}$$

where $u' = u - \langle u\rangle$, $\langle u\rangle$ is the time averaged velocity computed over the 25 days of the analysis window, and z_o is the depth level at which the velocity has been estimated by the reconstruction process. The time average is chosen to correspond to the entire analysis period since the stratification is approximately stationary in a statistical sense.

To compute C in Eq. (1), we concentrate on the area where the velocity difference between the EAS-16 and the LAVA estimations is significant, i.e., in the region of influence of the drifters (Fig. 6(a)). Since the water depths vary inside this region, we divide the region into six sub-regions according to the water depth (Fig. 6(b)). Then the function C is horizontally averaged inside each sub-region to find six vertical profiles (Molcard et al., 2005) as shown in Fig. 6(c) and (d).

The vertical correlation is then used to estimate the vertical projections of velocity corrections, $\Delta\mathbf{u}$,

$$\Delta\mathbf{u}(x,y,z,t) = \Delta\mathbf{u}(x,y,z_o,t)\cdot C_{z_o}(x,y,z), \tag{2}$$

where $\Delta\mathbf{u}(x,y,z_o,t) = u_e(x,y,z_o,t) - u_{mod}(x,y,z_o,t)$, and $u_e(x,y,z_o,t)$ is the velocity estimated by LAVA, while $u_{mod}(x,y,z_o,t)$ is the EAS-16 velocity.

The vertical projection of the estimated velocity field is then found from

$$\mathbf{u}_e(x,y,z,t) = \mathbf{u}_{mod}(x,y,z,t) + \Delta\mathbf{u}(x,y,z,t). \tag{3}$$

In Fig. 7, one example of the vertically projected estimated velocity corrections at 150 m is compared to the corresponding velocity corrections at the drifter level. The general pattern is similar between the two depths, while the strength is weaker at the deeper level.

3.2. Constrained normal mode analysis (NMA)

The Normal Mode Analysis (NMA) data blending technique (Eremeev et al., 1992a) has been used to study flow in Lake Ontario

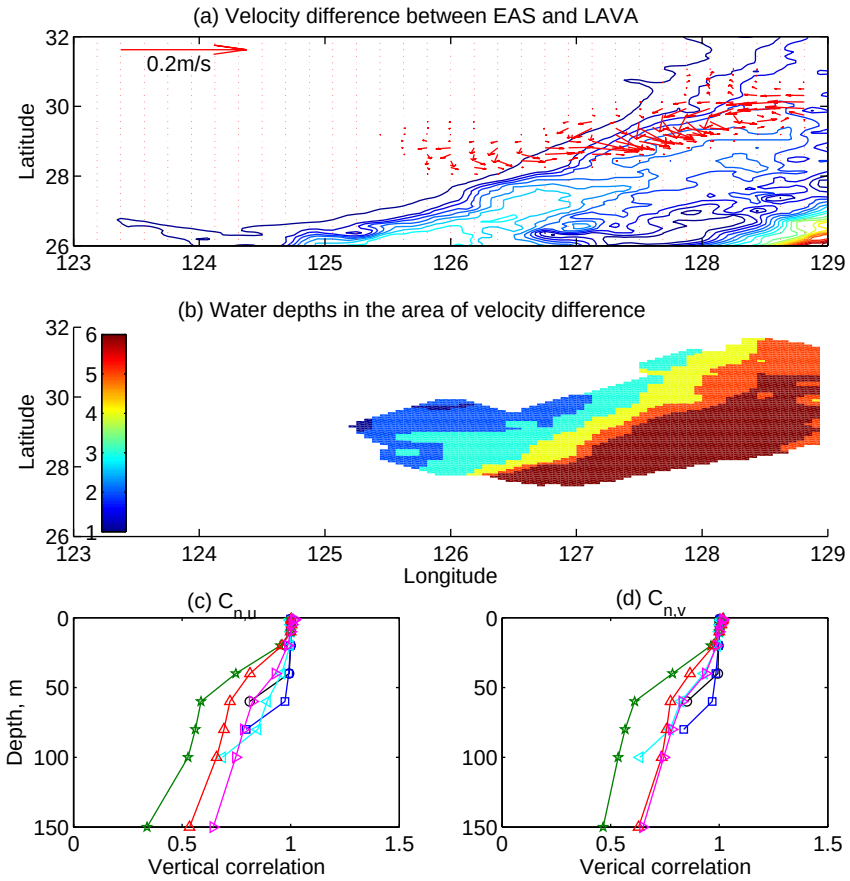

Fig. 6. (a) Velocity vectors that show the difference between EAS-16 and LAVA averaged over 25 days over bathymetry. The contours show the water depth ranging from 500 m (blue) to 3000 m (red). (b) Depth contours inside the region where the velocity difference is significant, defining six distinct sub-regions according to water depth h. Region 1: $h < 80$ m, Region 2: $80 \leqslant h < 100$ m, Region 3: $100 \leqslant h < 150$ m, Region 4: $150 \leqslant h < 400$ m, Region 5: $400 \leqslant h < 800$ m, Region 6: $h \geqslant 800$ m. (c) Vertical correlation profiles for the zonal velocity component u. (d) Vertical correlation profiles for the meridional velocity component v. Colors in the correlation plots correspond to the sub-regions defined in (b). (For interpretation of the references to colour in this figure legend, the reader is referred to the web version of this article.)

(Rao and Schwab, 1981), circulation in the Black Sea (Eremeev et al., 1992b), surface circulation in Monterey Bay (Lipphardt et al., 2000), among many other applications. The method has also been adapted to use drifter velocities to enhance near-surface model velocities in the Gulf of Mexico (Toner et al., 2001). Here, we follow Toner et al. (2001), using velocities derived from drifter trajectories to constrain NMA objective mappings of model velocities at one depth. An overview of the methodology and the parameter choices is provided here, while details are given in Appendix B.

The velocity field $\mathbf{u}$ is decomposed into the sum of a boundary solution $\mathbf{u}_{bdry}$, a set of Dirichlet modes $\mathbf{u}_n^D$, and a set of Neumann modes $\mathbf{u}_m^N$ (see details in Appendix B). Dirichlet modes are eigenfunctions of the Helmholtz equation with Dirichlet boundary conditions, while Neumann modes are eigenfunctions of the Helmholtz equation with Neumann boundary conditions. Thus, the velocity estimate is given by

$$\mathbf{u}_e(x,y,t) = \mathbf{u}_{bdry}(x,y,t) + \cdots \sum_{n=1}^{N_D} a_n(t)\mathbf{u}_n^D(x,y) + \sum_{m=1}^{N_N} b_m(t)\mathbf{u}_m^N(x,y), \quad (4)$$

where N_D is the number of Dirichlet modes and N_N is the number of Neumann modes, and a_n and b_m are the coefficients. The boundary solution is determined separately by matching normal flow on the boundary and solving for the velocity potential.

The coefficients are determined as the solution to a least squares problem minimizing

$$\|\mathbf{u}_e - \mathbf{u}_{mod}\|, \quad (5)$$

where $\|\cdot\|$ denotes the 2-norm. (This is equivalent to the minimization problem (B.10).)

NMA has several useful properties: it reduces the number of degrees of freedom, identifies the dominant length scales in a dynamic region, and applies systematic spatial smoothing through the choice of a length scale cut-off for the eigenfunctions. It can also be applied to irregularly spaced data and data from disparate sources, which is of primary importance in our context. There are various choices for the introduction of the observed velocities. At one end of the spectrum, they can be treated identically to the model velocities, introducing additional components to the cost function. In many cases, however, observations are taken to be more certain, and this can be accounted for in the set-up of the minimization problem through differential weighting. At the other end of the spectrum—the method employed here—the observations are imposed as hard constraints on the cost function.

The primary parameter that enters the set-up of this type of NMA is the choice of the number of modes or the minimum resolved length scale. If too few modes are used, the solution may be forced to be smoother than is realistic. At the same time, the hard constraints may result in undesirable large-scale spatial oscillations. (In the extreme case, the constrained minimization has no solution.) On the other hand, if too many modes are used, then, in

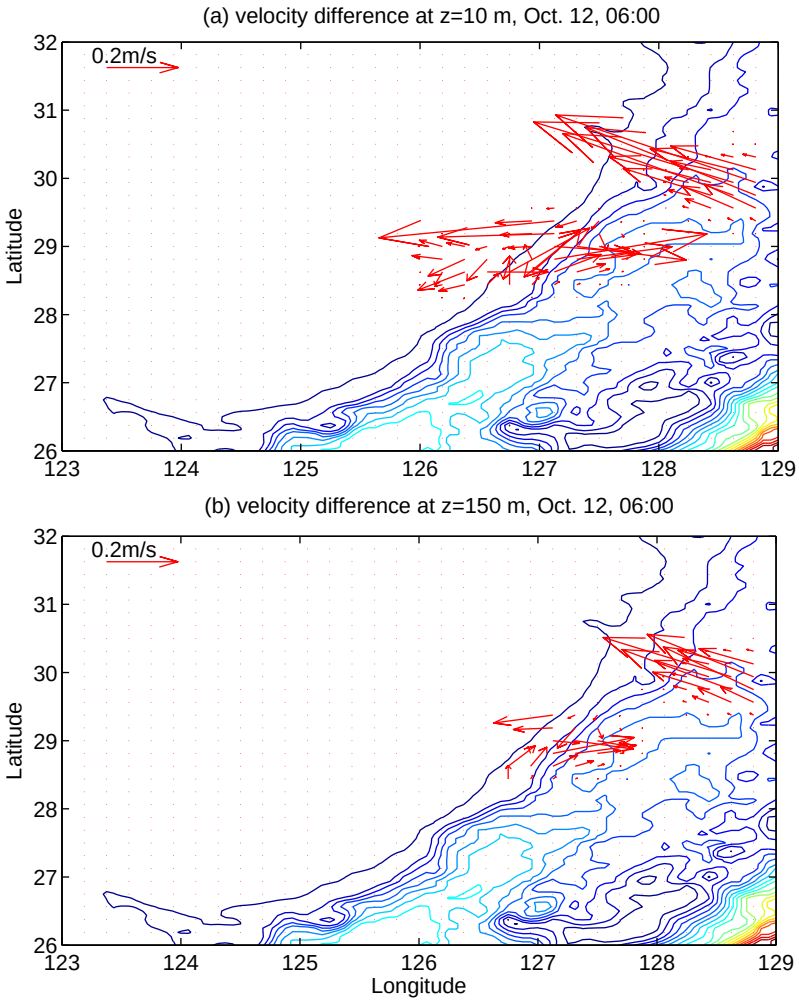

Fig. 7. Velocity difference between EAS-16 and LAVA at (a) the drifter level and (b) the vertical projection at $z = 150$ m, over bathymetry. The contours show the water depth ranging from 500 m (blue) to 3000 m (red). This example is taken at 6:00 Oct. 12, 2007. (For interpretation of the references to colour in this figure legend, the reader is referred to the web version of this article.)

effect, the model is weighted more heavily and may reduce the sphere of influence of each observation too much. Choosing the correct length scale cut-off to minimize spurious long distance effects yet maximize meaningful impact of the observations is something of an inexact art, usually involving some trial and error.

Here we have chosen the length scale cut-off to be at 0.125°, the equivalent of twice the grid spacing, and the domain 125.5°–128.5° E by 27.75°–30.75° N. This results in $N_D = 576$ Dirichlet and $N_N = 624$ Neumann modes. Given such a rich data set of observations as the LWAD07 SVP drifters, we actually have on occasion multiple observations that are closer than the smallest resolved spatial scale. While the machinery of NMA is capable of solving the constrained least squares minimization nonetheless—due to the large number of modes relative to the number of observations—the result is not necessarily sensible. Consequently, we implement a filter on the observations, imposing 0.125° as the minimum distance between included data points.

Theoretically, it is possible to extend NMA into three dimensions and carry out a three-dimensional constrained minimization. However, this is computationally costly. As all observations in our case are restricted to a single depth, we apply a constrained NMA to the nearest model level (10 m) and project the innovations down (and up) in the water column using linear regression. At each time, an unconstrained NMA map is found for all levels, in addition to the constrained NMA map for the reference level. For each non-reference level separately, a linear regression coefficient C is determined for each of the amplitudes for each 24 h window, relative to the corresponding reference level amplitudes (Eq. (6)). This coefficient is used to project the innovation increment from the reference level to the other level, which is then added to the unconstrained NMA map of the non-reference level (Eq. (7)). Mathematically, this process can be summarized as follows, where $\mathbf{a}$ represents an amplitude time series, k indexes the amplitudes, z_o refers to the reference level, subscript e marks amplitude estimates from the constrained NMA, primes indicate perturbations from a 24-h mean, and superscript T denotes the matrix transpose:

$$C_{z_o}(k,z) = \frac{\mathbf{a}'(k,z)^T \mathbf{a}'(k,z_o)}{\mathbf{a}'(k,z_o)^T \mathbf{a}'(k,z_o)}, \tag{6}$$

$$\mathbf{a}_e(k,z) = \mathbf{a}(k,z) + C_{z_o}(k,z)(\mathbf{a}_e(k,z_o) - \mathbf{a}(k,z_o)). \tag{7}$$

This method of statistical projection is identical to that described in Section 3.1, with two exceptions: (1) The correlation is carried out on NMA amplitudes instead of directly on the velocities, and (2) the time average is taken over 24 h instead of over 25 days.

Note that the boundary solution of neither the reference level nor any other level is affected by the observations. This is a limitation of the NMA method, but does not cause too much trouble as long as the boundary of the domain used is far enough away from the area of interest, a typical restriction to avoid unintended boundary effects (for more details, please refer to Appendix B).

The method has been applied to create hourly NMA velocity fields for the time period from 12:00 October 8, 2007 to 11:00 October 15, 2007. The first observation is available for 22:00 October 8, 2007, from which point onwards the constrained NMA algorithm is used. The number of observations blended each hour varies from 1 to 14. Recall that spatial filtering of observations was applied to avoid imposing unresolved spatial variability. Consequently, the full set of thirty drifters was never used, even during the period when all were reporting.

The chosen least resolved spatial scale is fairly small, so that the impact of the observations remains somewhat localized. This is, of course, particularly true when few observations are absorbed. Fig. 8 shows the velocity fields from the original EAS-16 model and from the constrained NMA, as well as the differences in the fields, for two sample days with 5 and 13 observations used, respectively. Fig. 9 illustrates the effects on a deeper level, in this case the one at 40 m. We can see that at the lower levels, too, the corrections are restricted to the geographic area immediately near the observations but are smaller than at the reference level. Both of these characteristics are desirable, since velocities at depth tend to be smaller.

3.3. Internal consistency tests using drifter trajectories

A first test on the corrected velocity fields obtained with the two methods in Sections 3.1 and 3.2 is performed comparing synthetic trajectories with the observed in situ drifter trajectories. Since the velocity correction is based on the drifter data themselves, the test is mostly aimed at verifying internal consistency, and a significant improvement is expected to occur for the trajectories in the corrected fields with respect to the original EAS-16 ones.

The synthetic trajectories are numerically advected using the model velocity fields starting from the launch locations of the in situ drifters. Fig. 10 shows two-day trajectories after the launches based on the following fields: EAS-16 (red, left panel), NMA corrected (blue, center panel), and LAVA corrected (green, right panel). In all the panels, the synthetic trajectories are shown together with the in situ ones (black). It is evident from visual inspection that both methods lead to a substantial improvement. The NMA and LAVA trajectories appear significantly closer to the observations than the EAS-16 ones, capturing the two different flow regimes, on the shelf and in the Kuroshio, respectively. The corrected trajectories on the shelf are characterized by tidal motion and reduced drift, while those caught in the Kuroshio exhibit a swift northeastern drift, similar to the observations.

This result is quantified by computing the rms error in the modeled versus observed positions, averaged over all the available drifters, as a function of time:

$$E = \sqrt{\frac{1}{N_{drift}} \sum_{n=1}^{N_{drift}} \|\mathbf{r}_{obs}(n) - \mathbf{r}_{mod}(n)\|^2}, \tag{8}$$

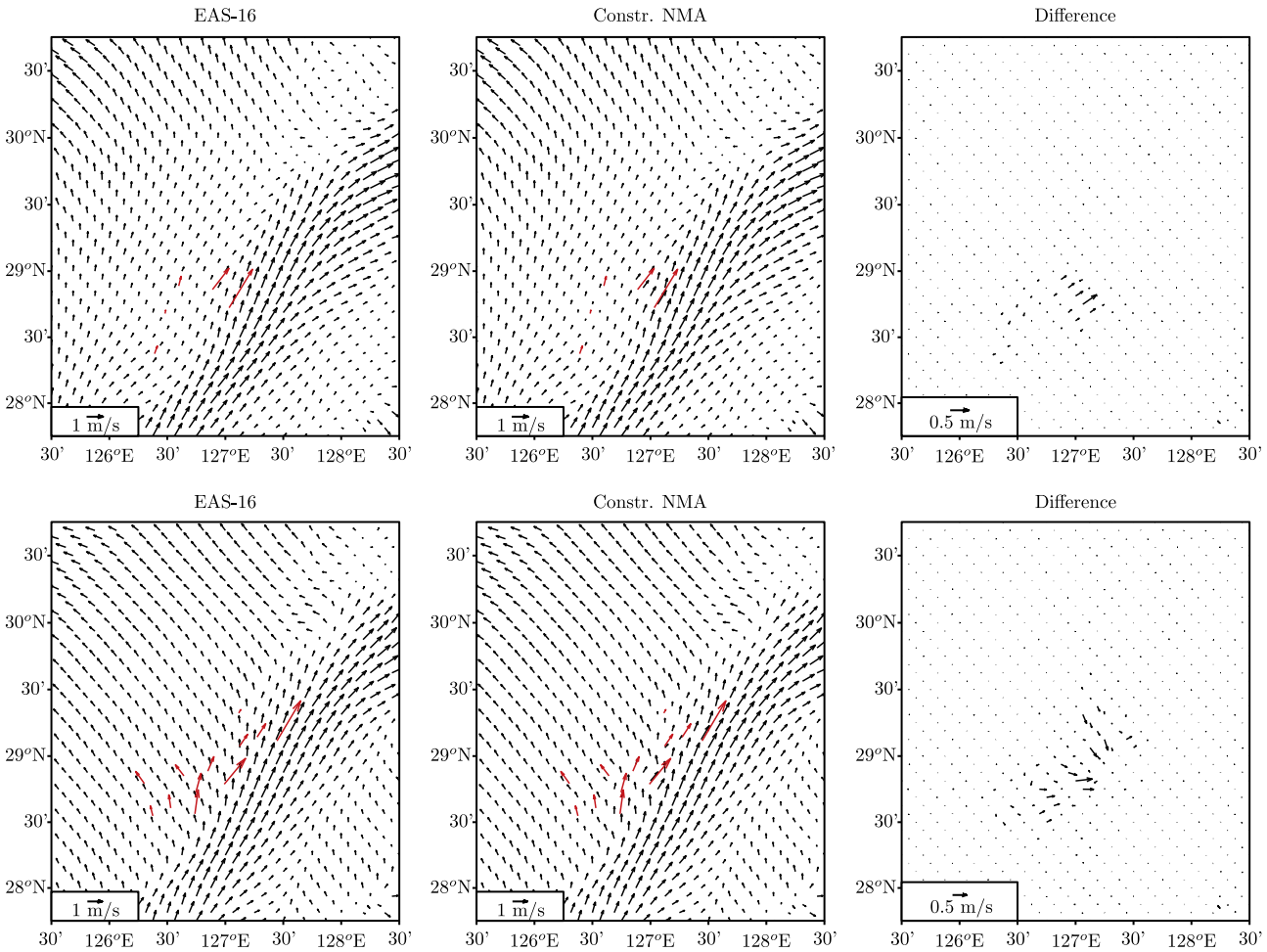

Fig. 8. Comparison of velocity fields at the 10 m reference level from (left) EAS-16 and (middle) constrained NMA. The panels on the right depict the differences (NMA − EAS-16); note the different vector scale used there. Red arrows show the assimilated observations. The top three panels are for 12:00 October 9, 2007, when only five observations were used, while the lower three panels are for 12:00 October 12, 2007, when 13 observations were used. (For interpretation of the references to colour in this figure legend, the reader is referred to the web version of this article.)

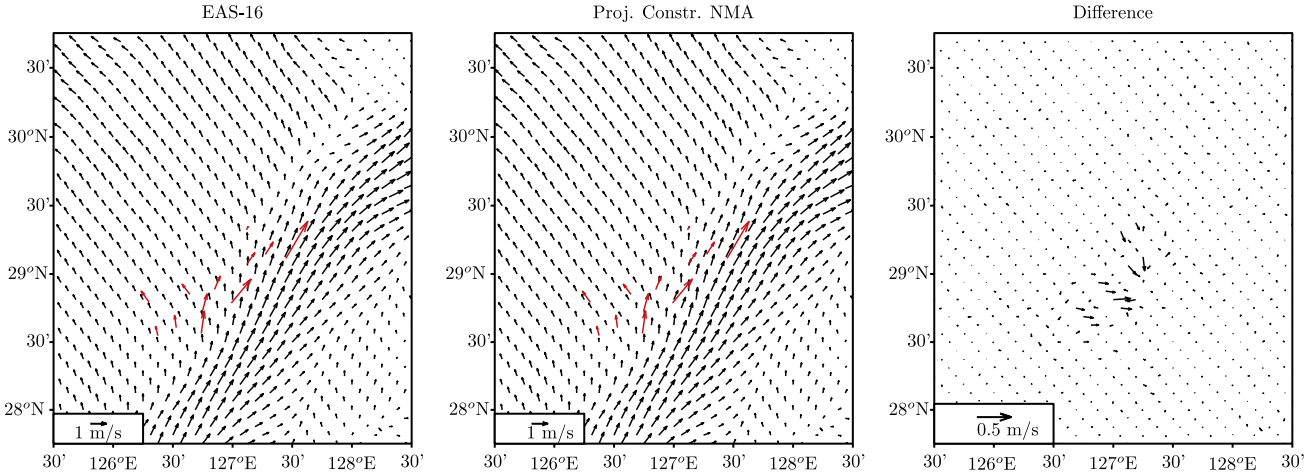

Fig. 9. Comparison of velocity fields at the 40 m level from (left) EAS-16 and (middle) projected constrained NMA. The panels on the right depict the differences (NMA − EAS-16); note the different vector scale used there. Red arrows show the assimilated observations. These plots are for 12:00 October 12, 2007, like the bottom panels in Fig. 8. (For interpretation of the references to colour in this figure legend, the reader is referred to the web version of this article.)

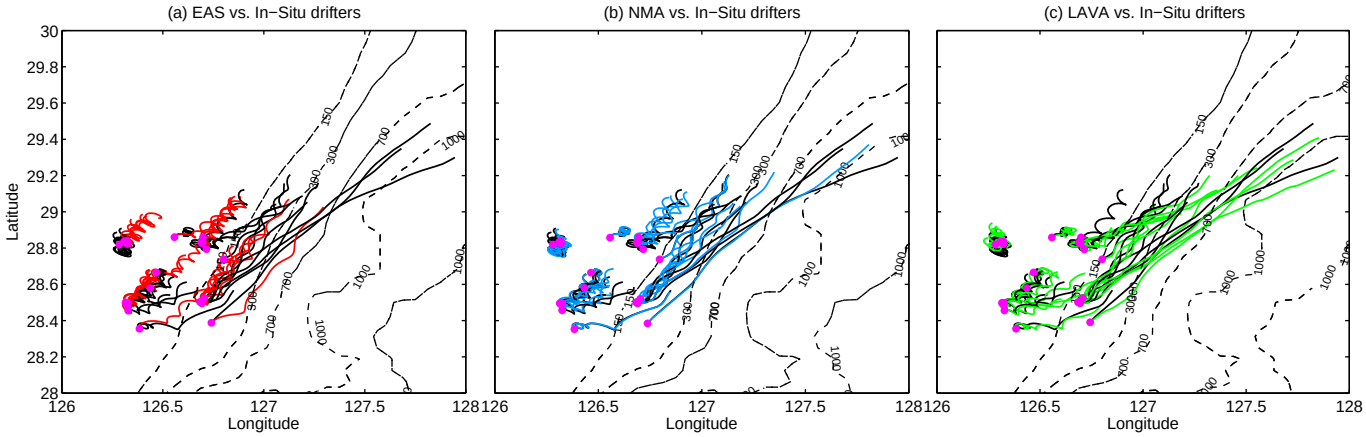

Fig. 10. Modeled drifter trajectories using the EAS-16 (red, a), NMA corrected (blue, b), and LAVA corrected (green, c) model velocity fields, compared to in situ data (black) over two days following launches. Purple circles mark initial locations. (For interpretation of the references to colour in this figure legend, the reader is referred to the web version of this article.)

where $\mathbf{r}_{obs}(n)$ and $\mathbf{r}_{mod}(n)$ are the positions of the nth observed and modeled trajectories, respectively, at the set time and N_{drift} is the number of drifters available at that time. The error for the three sets of trajectories computed from EAS-16, NMA, and LAVA, respectively, are shown in Fig. 11, where the standard deviation σ is also plotted to indicate the range of the trajectory errors. While the EAS-16 error (red line) increases almost linearly, reaching approximately 21 km after 24 h, the NMA and LAVA curves (blue and green, respectively) show a slower rate of growth, reaching approximately 9.5 km for NMA and 5.5 km for LAVA after 24 h.

Fig. 12 displays the separation distance as a function of time for the individual drifters between the observed trajectory and that modeled by each of the methods.Note that the distributions across drifters are skewed with a tail at the upper end. Separation distances for each of the improved models are more clustered towards the lower end.While NMA has more trajectories that stay within 3 km of the observations after 24 h (18) than LAVA (10), it also results in larger excursions with a maximum of 27.5 km, versus 17.1 km for LAVA.

We characterize the improvement or gain due to the corrected velocities with a simple bulk metric G, given by the normalized difference between the rms errors at 24 h for the EAS-16 and the corrected models. The 24 h horizon is chosen as particularly relevant for operational applications. This provides the following values for NMA and LAVA, respectively:

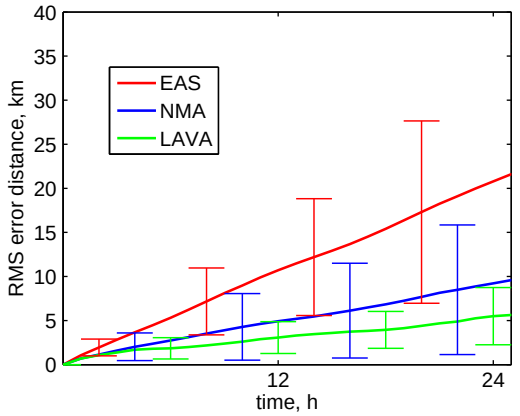

Fig. 11. Comparison of rms errors for drifter trajectories modeled using EAS-16 (red), NMA corrected (blue) and LAVA corrected (green) velocity fields. Time is measured from each drifter's launch. Error bars show ± one standard deviation. (For interpretation of the references to colour in this figure legend, the reader is referred to the web version of this article.)

$$G_{NMA} = 1 - E_{NMA}/E_{EAS} \approx 55\%, \quad (9)$$

$$G_{LAVA} = 1 - E_{LAVA}/E_{EAS} \approx 75\%. \quad (10)$$

4. Assessment of velocity reconstruction using sonobuoy trajectories

The corrected velocity fields obtained using SVP drifter data as described in Section 3 are quantitatively tested here against data from the CDMR sonobuoy trajectories. The testing methodology is similar to the one used in Section 3.3, i.e. synthetic trajectories are computed based on the velocity fields and compared with the observed trajectories. There is, however, a conceptual difference between the present analysis and the one performed in Section 3.3 using drifters, since the sonobuoy trajectories provide an independent data set, that has not been used in the velocity reconstruction. We recall that sonobuoy trajectories differ significantly from the drifter ones (see Fig. 3) due to different depth dependent drag and different initial conditions. The comparison performed here therefore provides an independent quantitative test of the quality of the reconstructed velocities.

Synthetic sonobuoy trajectories are calculated using the Sonobuoy Field Drift Model (SFDM), see Hammond (2005, 2008a,b) and Appendix C for details. The code was developed as a Navy mission planning tool under the ODDAS (Optimal Deployment of Drifting Acoustic Sensors) program. SFDM models the hydrodynamic response of sonobuoys—represented as a distributed series of surface and subsurface drag/mass bodies and cable—to a spatially and temporally varying water velocity field. While aerodynamic drag on the surface buoy is an integral part of the model, no wind drag was taken into account here, since wind field data was not available. However, over 90% of the drag area of a typical sonobuoy lies below the surface of the water, and previous studies (Coughlan, 1975) have shown that wind typically contributes less than 2% to the sonobuoy drift.

SFDM simulations were conducted for the LWAD07 sonobuoy deployments using the three model velocity fields: EAS-16, NMA corrected, and LAVA corrected. These modeled trajectories in comparison to those from the observed sonobuoy data are plotted in Fig. 13. Qualitatively the SFDM modeled results using the corrected velocity fields show better correlation to the in situ data. As for the drifter data in Fig. 10, the EAS-16 predictions tend to be fairly uniform in space, whereas both of the corrected velocity fields are better able to predict the looping behavior of the sonobuoys deployed in the northwestern corner, while also increasing the energy of the trajectories in the southwestern corner and in the Kuroshio (even though the drift of the current is still underpredicted).

The separation distance Δ between the in situ data and the SFDM results is computed for all trajectories and plotted as a function of time in Fig. 14 for the entire operating life of each sonobuoy. This data supports the qualitative conclusion that the corrected velocity fields improve the sonobuoy drift predictions. While the majority of the sonobuoy trajectories predicted using the corrected velocity fields (blue and green) exhibit separation distances less than 20 km over the whole life span, there are very few trajectories with distances consistently less than 20 km when the EAS-16 output (red) is used for SFDM predictions.

In Fig. 15, the rms separation distance averaged over all trajectories, corresponding to the error E defined in Eq. (8), is shown for each of the model velocity fields. Notice that $E(t)$ tends to plateau for all velocities after approximately 20 h, at which point a few trajectories with high errors die, as shown by the individual $\Delta(t)$

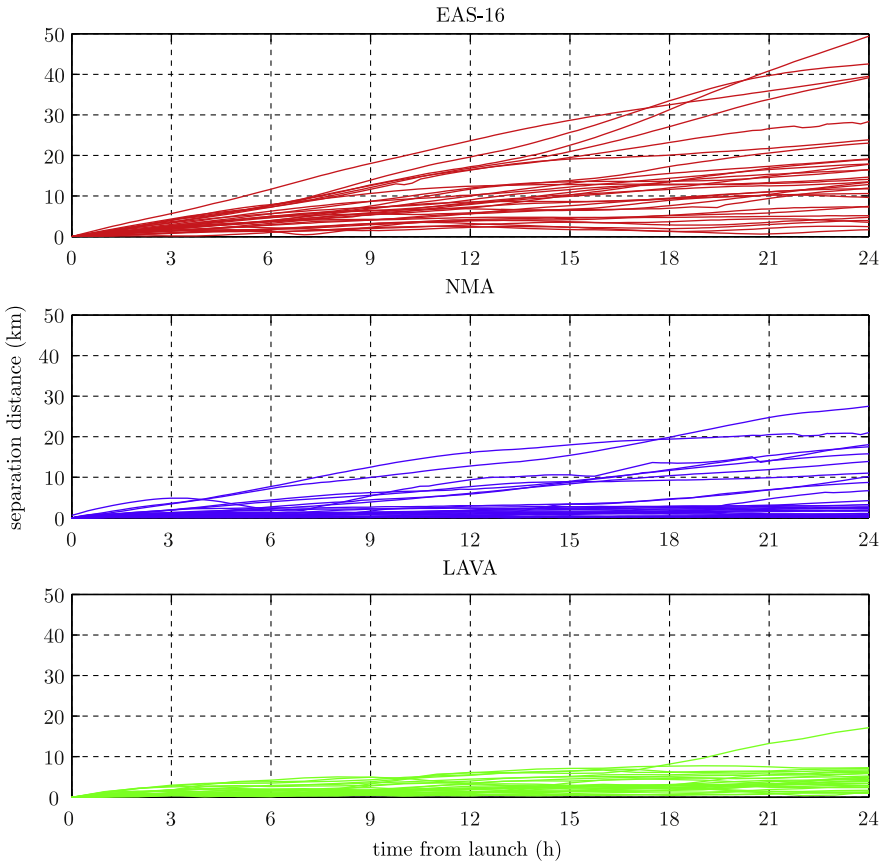

Fig. 12. Timeseries of separation distances between in situ and modeled drifter trajectories using EAS-16 (red), NMA corrected (blue), and LAVA corrected (green) velocity fields. (For interpretation of the references to colour in this figure legend, the reader is referred to the web version of this article.)

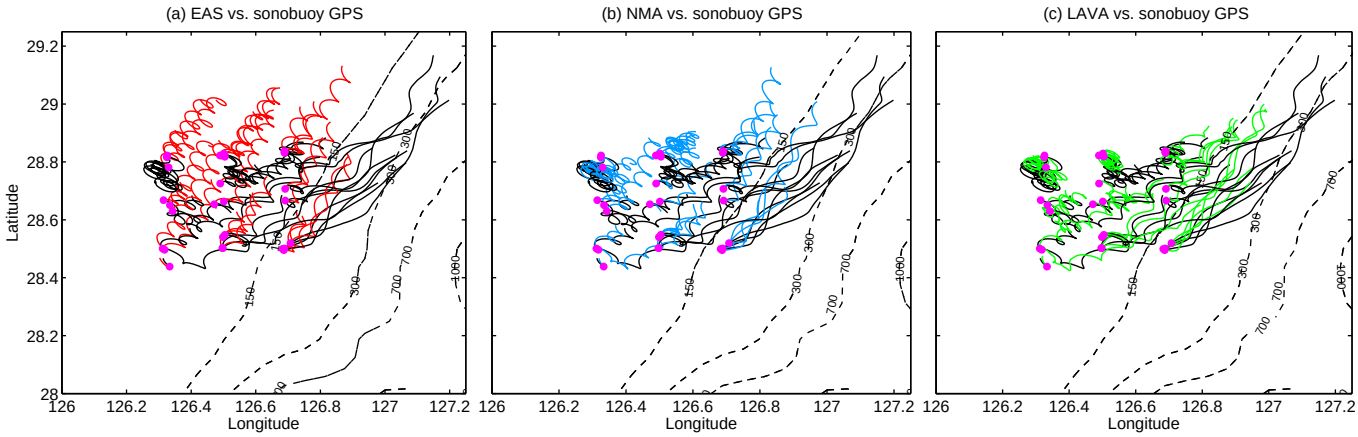

Fig. 13. Modeled (SFDM) sonobuoy trajectories using the EAS-16 (red, a), NMA corrected (blue, b) and LAVA corrected (green, c) model velocity fields, compared to in situ data (black) for two days after deployment. Purple circles mark initial locations. (For interpretation of the references to colour in this figure legend, the reader is referred to the web version of this article.)

in Fig. 14. Both the NMA and LAVA corrected velocity fields show a significantly improved performance over the EAS-16 results.

The gain at 24 h is computed from E as in Section 3.3, giving for NMA and LAVA, respectively,

$$G_{NMA} \approx 25\%, \tag{11}$$

$$G_{LAVA} \approx 50\%. \tag{12}$$

These values are smaller than those obtained in Section 3.3 for drifters, as is expected, given that the sonobuoy data are not used in the reconstruction. The decrease is relatively small, though, on the order of 25% for both fields, suggesting that the results of the methods are robust and provide useful results not only at the drifter level but also throughout the water column.

Another practical metric to characterize the performance is the time to separation τ_L for some distance, L, between the modeled and in situ trajectories. For the purposes of this study a distance of roughly 2 grid spacings or 15 km has been chosen for L. The τ_{15} metric cannot be used to make average comparisons of overall field performance, since in many cases the sonobuoy reaches the end of its life (EOL) before separating more than 15 km from the modeled trajectories. However, it can be used to compare the performance for individual sonobuoys.

It is instructive to examine some specific examples to illustrate the effectiveness of using the corrected velocity fields for sonobuoy drift prediction. The following three examples demonstrate typical behavior of sonobuoys deployed in three regions of the test area. The in situ data and SFDM results using the three model velocity fields are plotted together and the separation distance at 24 h, Δ_{24}, as well as the τ_{15} metric are compared.

Buoy #1 is shown in Fig. 16. This sonobuoy was deployed in the transition region between the two regimes of the shelf and of the

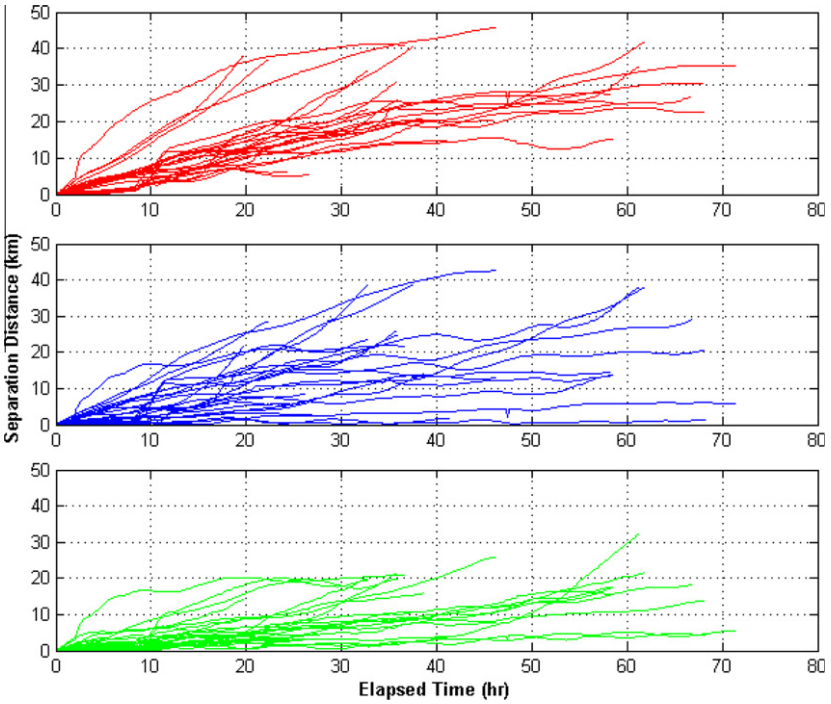

Fig. 14. Timeseries of separation distances between in situ and modeled (SFDM) sonobuoy trajectories using EAS-16 (red), NMA corrected (blue), and LAVA corrected (green) velocity fields. (For interpretation of the references to colour in this figure legend, the reader is referred to the web version of this article.)

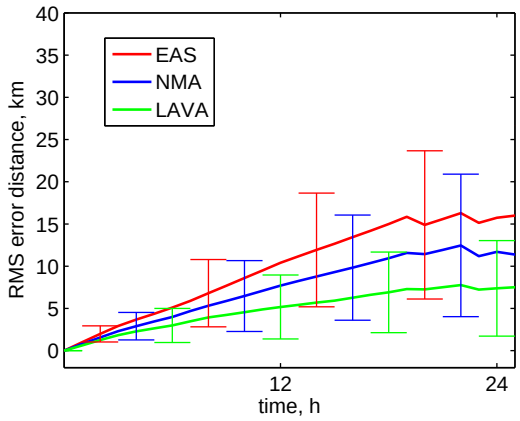

Fig. 15. Comparison of rms errors for modeled sonobuoy trajectories (SFDM) using EAS-16 (red), NMA corrected (blue), and LAVA corrected (green) velocity fields. Time is measured from each sonobuoy's launch. Error bars show ± one standard deviation. (For interpretation of the references to colour in this figure legend, the reader is referred to the web version of this article.)

Kuroshio. Here the in situ data show that the sonobuoy initially moved to the southeast before getting caught up in the Kuroshio and drifting rapidly to the northeast. The drift predictions using the EAS-16 velocity field data do not capture this type of motion. The 24-h separation distance is almost 14 km increasing to 41 km by the end of the buoy's life (61.5 h). However, drift predictions made using either corrected velocity field do exhibit the correct drift pattern. At 24 h both predictions show low separation distances. Drift velocity using the corrected velocity fields is generally lower than observed once the sonobuoy is in the Kuroshio, and separation distance increases over the life of the buoy. The LAVA predictions show better performance in this case than the NMA predictions, staying within 15 km of the observed position for over 51 h, versus about 41 h using NMA corrected velocity fields and 26 h for EAS-16.

Buoy #8 (see Fig. 17) was deployed in the southeast corner of the test site where the influence of the Kuroshio was dominant. After initially drifting to the ENE at a high velocity for roughly the first 8 h, Buoy #8 slows slightly and drifts NNE until it dies. None of the SFDM results predict the initial ENE motion. All three data sets do predict that Buoy #8 will drift to the NNE, although at a lower velocity than the observed data. This initial divergence is why none of the predicted trajectories were able to remain within 15 km of the observed data for more than 10.2 h. Nonetheless, due to the better drift speed correlation, the corrected velocity predictions show significant improvement in separation distance after 24 h: 37.3 km with the EAS-16 output and roughly 20 km for both corrected velocity fields.

Buoy #18 is plotted in Fig. 18. This buoy was deployed in the northwest corner of the test site. As was typical for sonobuoys deployed in that region, it was observed to loop with a semi-diurnal period and slow mean translation to the southwest. The SFDM results using the EAS-16 velocity field fail to replicate this motion. Although there is a semi-diurnal looping present, there is a significant mean translation to the northeast such that by the end of the buoy life (68 h) the EAS-16 predicted position is over 30 km from the observed. The corrected velocity field predictions perform much better, as they capture the general character of the observed motion. Separation distances are more a function of phase differences in the elliptical motion between the predicted and observed positions. The NMA corrected results indicate separations distances less than 1.5 km for the life of the buoy, while the LAVA corrected results remain less than 5 km from observations.

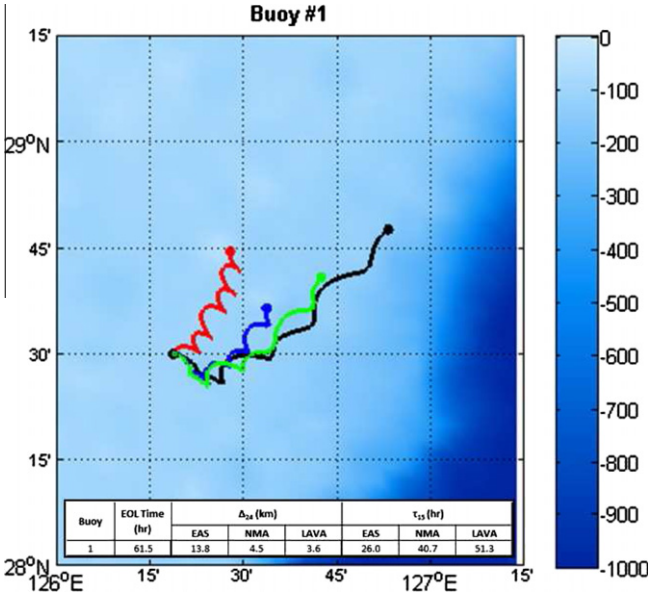

Fig. 16. Plot of observed sonobuoy trajectory (black) and SFDM modeled trajectories using EAS-16 (red), NMA corrected (blue), and LAVA corrected (green) velocity fields for Buoy #1. Bathymetry is shown in shades of blue (in m). (For interpretation of the references to colour in this figure legend, the reader is referred to the web version of this article.)

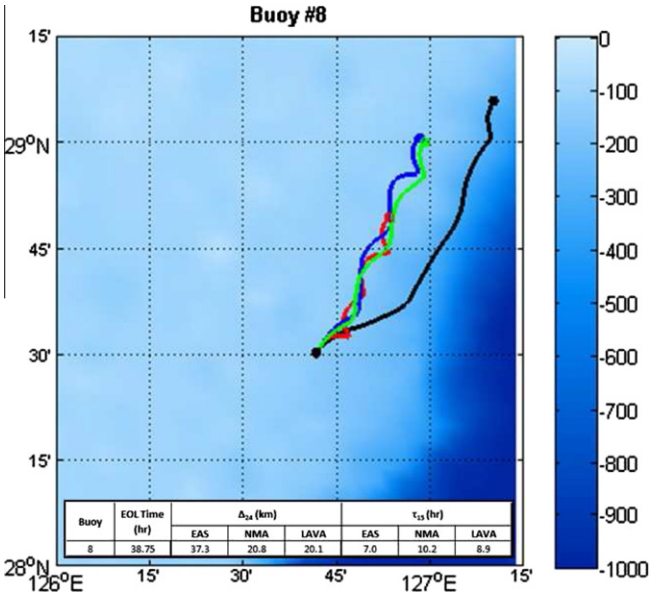

Fig. 17. Plot of observed sonobuoy trajectory (black) and SFDM modeled trajectories using EAS-16 (red), NMA corrected (blue), and LAVA corrected (green) velocity fields for Buoy #8. Bathymetry is shown in shades of blue (in m). (For interpretation of the references to colour in this figure legend, the reader is referred to the web version of this article.)

The performance of the three models is summarized in Table 1 for each of the sonobuoys deployed during LWAD07 in terms of separation distance after 24 h and at the end of the sonobuoy life.

5. Summary and concluding remarks

In this paper we provide a quantitative assessment of the improvement in trajectory prediction obtained with velocity fields corrected using Lagrangian data. We consider the specific application

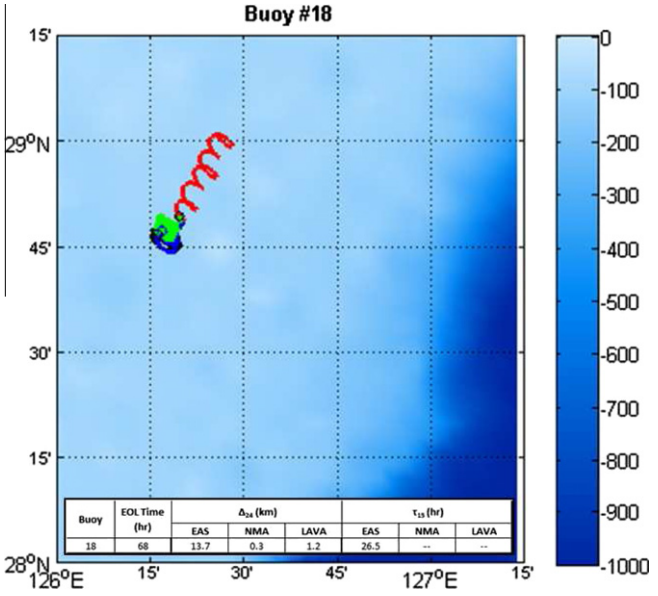

Fig. 18. Plot of observed sonobuoy trajectory (black) and SFDM modeled trajectories using EAS-16 (red), NMA corrected (blue), and LAVA corrected (green) velocity fields for Buoy #18. Bathymetry is shown in shades of blue (in m). (For interpretation of the references to colour in this figure legend, the reader is referred to the web version of this article.)

of predicting sonobuoy trajectories launched during the LWAD07 experiment off Taiwan.

The velocity fields of the data assimilating model EAS-16 are corrected using data from SVP drifters launched during the same time period and drogued at 15 m. The corrections are statistically propagated from the drifter depth throughout the water column using the statistics of the (uncorrected) EAS-16 fields. Synthetic sonobuoy trajectories are then computed from the EAS-16 and from the corrected velocity fields using an appropriate drift model that describes the hydrodynamic response of sonobuoys in terms of distributed drag in the upper 27 m, and the synthetic trajectories are quantitatively compared with the observed ones. The region of interest is especially challenging since it is situated at the edge of the Kuroshio. Both drifter and sonobuoy data sets show the presence of two distinct flow regimes occurring in a restricted domain (order of 1/2° square) and separated by a sharp transition area. The western side is characterized by shelf dynamics with a significant tidal component, while the more eastern part is dominated by the highly energetic meandering of the Kuroshio. The drifter and sonobuoy data sets, even though qualitatively similar, have significant quantitative differences, with the sonobuoy trajectories being overall slower and exhibiting slightly different orientations. This is likely due to the fact that sonobuoys respond differently to currents at different depths and that they have been launched at slightly different points and times than the drifters. The EAS-16 model does not capture the presence of the two regimes, and its synthetic trajectories show a more homogeneous northeastward motion with a strong tidal component. This is not surprising, given the high nonlinearity of the flow, that makes its detailed structure difficult to predict, and the small size of the target area with respect to the resolution of the assimilation observing system.

Two different methods for velocity reconstruction have been considered. One method, LAVA, is based on a variational approach. It corrects the velocity field by requiring minimization of the distance between observed and modeled trajectories. The other method, NMA, is based on an expansion into normal modes. It uses the velocities computed along the trajectories as hard constraints on the cost function.

The results are qualitatively compared with the observations by visual inspection of the trajectories. A quantitative analysis is then performed, considering as main metric the rms separation (error) between the observed and synthetic trajectories after 24 h. Another metric is also considered, namely the time to separation between observed and synthetic trajectories of 15 km (roughly corresponding to twice the model horizontal grid spacing).

We first test for internal consistency of the two methods, considering the SVP drifter trajectories. While the EAS-16 trajectories do not reproduce the two dynamical regimes, the trajectories based on the corrected fields appear quite similar to the observed ones and show the significant difference between the two regimes. The error is decreased, with a gain of approximately 75% for LAVA and 55% for NMA. An improvement is indeed to be expected, since the fields are corrected based on the drifters. Nevertheless, our analysis provides a quantitative test that the methods produce consistent results.

We then consider the independent sonobuoy data set and perform a similar trajectory comparison. As for the drifters, both LAVA and NMA based trajectories are qualitatively much more similar to the observed ones than the EAS-16 based ones. Quantitatively, the error decreases less than for the drifters, but still significantly: approximately 50% for LAVA and 25% for NMA. For the separation time metric, a bulk value for the whole data set cannot be computed since many trajectories do not reach a separation of 15 km during their entire life (which is on the order of two days). Comparisons are performed considering single trajectories, and a significant general improvement is found for both LAVA and NMA with respect to EAS-16. Best results appear to be obtained for both methods for trajectories situated on the shelf, whose velocities tend to be overestimated by the model. The drifter-based correction reduces the average velocity on the shelf, and the resulting trajectories tend to loop almost in place, in keeping with the observations. Trajectories in the Kuroshio are on average more energetic thanks to the correction, although in some cases not energetic enough compared to the observed ones. The correction in the Kuroshio region might be less effective due to the fact that drifters there move very quickly, resulting in sparser coverage, not always adequate for the correction.

Both methods produced significant improvement in reconstructing the sonobuoy trajectories. Even though based on two completely different approaches, they provide qualitatively similar results. Quantitatively, LAVA provides a greater error reduction. This is likely due to at least two factors. Results from previous work (Molcard et al., 2003) show that trajectory-based corrections are generally more effective than corrections relying on derived velocities, at least when the time steps of correction are a sizable fraction of the Lagrangian time scales T_L, as in this case. Conceptually this is due to the fact that Eulerian and Lagrangian velocities are different at those scales and the Lagrangian observational operator is more appropriate, allowing the minimization of the difference between observed and modeled trajectories.

A more specific difference between the methods is that the NMA methodology used here imposes a hard constraint, requiring that the reconstruction exactly matches the drifter observations, while LAVA optimally weighs the observations with no such requirement. Hence LAVA allows for some error in the observations whereas NMA does not. A further consequence of this particular formulation of NMA is that not all the available data is ingested: At most 14 of the 30 drifters were used at any one time. In addition, NMA results in a more localized correction than LAVA. Of course, NMA can be readily adapted to permit observational error by converting the constrained optimization into a weighted optimization problem. This would likely improve its performance. LAVA, moreover, could probably be further optimized as well. The present purpose, however, was to demonstrate

Table 1
Summary of separation distance between modeled and observed sonobuoy trajectories after 24 h and at end of buoy life for all three velocity fields. (Note that Buoy # 22 never deployed and is hence not listed below.)

Buoy	Lifespan (h)	Separation distance after 24 h (km)			Separation distance at EOL (km)		
		EAS-16	NMA	LAVA	EAS-16	NMA	LAVA
1	61.50	13.8	4.5	3.6	41.4	37.5	21.3
2	24.50	6.1	5.8	2.5	6.3	6.0	2.4
3	*22.00*	*n/a*	*n/a*	*n/a*	*36.3*	*28.3*	*9.4*
4	27.25	11.5	5.6	4.4	14.2	7.3	4. 6
5	26.00	13.5	7.6	2. 9	15.2	8.6	3.0
6	35.75	13.9	16.4	18.7	25.9	24.7	19.8
7	41.25	9.4	0.4	2.5	14.8	1.8	3. 8
8	38.75	37.3	20.8	20.1	40.9	21.7	20.8
9	68.00	13.9	14.1	5.0	22.5	204	13.7
10	*11.25*	*n/a*	*n/a*	*n/a*	*7.1*	*5.8*	*3.1*
11	46.00	31.6	27.3	9.3	45.5	42.5	25.8
12	38.75	9.2	5.1	10.0	19.7	13.9	15.9
13	64.25	8.6	6.7	4.9	15.2	13. 8	15.6
14	*19.50*	*n/a*	*n/a*	*n/a*	*37.5*	*21.0*	*13.9*
15	35.50	17.2	14.5	6.3	30.4	25.4	20.9
16	64.25	15.2	11.3	5.0	25.2	13.6	17.3
17	72.50	13.8	13.0	4.2	26.9	28.9	18.1
18	68.00	13.7	0.3	1.2	30.4	1.3	4.2
19	*6.75*	*n/a*	*n/a*	*n/a*	*4.1*	*2.0*	*1.2*
20	46.00	15.4	10.8	7.2	20.4	12.8	7.7
21	38.75	14.7	11.4	1.9	33.6	38.3	19.8
23	71.25	15.9	2.3	1.7	35.1	5.7	5.5
24	37.25	19.8	21.4	7.5	40.1	38.4	10.5
25	38.75	14.6	17.9	16.3	23.3	23.3	19.5
26	61.00	16.8	15.1	1.5	34.8	37.7	31.8
27	*5.25*	*n/a*	*n/a*	*n/a*	*1.1*	*0.6*	*1.1*
28	26.75	5.0	3.0	3.0	5.7	2.9	3.1
29	64.50	16.4	13.2	6.1	27.4	14.1	17.0

Highlighted rows correspond to the sonobuoys pictured in Figs. 16–18.
Italics indicate those buoys with a lifespan less than 24 h.

the utility of blending Lagrangian data with model velocities and not to compare competing methods or determine their optimal implementations.

Overall, the results show that the use of Lagrangian data to correct model velocity fields is a powerful tool to improve trajectory prediction. This suggests that in many practical applications, such as search and rescue or pollutant release problems, prediction could be improved by performing ad hoc launches of drifters and using the data to correct model results.

We stress that the velocity reconstruction as tested here has limited forecasting capabilities. True forecasts with Lagrangian assimilation require running the model forward starting from a corrected state, where the mass variables are also modified, consistently with the velocity field. Early examples of true forecasts from Lagrangian assimilations using Argo float data in the interior ocean, correcting the mass field based on dynamic principles in concert with mass conservation (Özgökmen et al., 2003), have been reported in Taillandier et al. (2006a, 2010). In this context, the use of a dynamically evolving correlation matrix between drifters, sonobuoys, and model velocities, as in the Extended or Ensemble Kalman filter, could provide further improvements in the forecast. In addition, an approach that computes covariances dynamically may be very useful for direct assimilation of sonobuoy trajectories. While desirable in specific applications, incorporating sonobuoy trajectories is expected to be more challenging than those of Argo floats and drifters, since they sample a significant portion of the upper ocean rather than a single level.

Several related issues have to be considered regarding assimilation of Lagrangian data sampling the upper ocean. First, Lagrangian sensors might sample submesoscale flows that can be present in the surface layers, but that might not be correctly resolved by the operational models. This raises the question of whether this data should be filtered to correct only the mesoscale component (as done for LAVA in the present paper), or submesoscale signatures should be retained or possibly used to improve model parameterizations. A second issue is that a simple geostrophic balance is not expected to hold and cannot therefore be used to correct the mass field as in Özgökmen et al. (2003). Upper ocean and mixed layer dynamics imply the presence of Ekman dynamics as well as possible strong nonlinearities related to fronts and submesoscale features. It seems to us that more knowledge is needed of such dynamics to guide a meaningful state correction for sequential data assimilation. Alternatively, this dynamic information could be incorporated implicitly in a forecasting system that computes the correlations as they evolve, for example from an ensemble analysis. Such an approach appears promising in scenarios where the dynamics are nonlinear and highly complex.

Acknowledgements

This research was supported by the Office of Naval Research under grants N00014-07-1-0730, N00173-08-1-GOO9, N00014-09-1-0559, N00014-09-1-0703 and the Mary A. S. Lighthipe endowment to the University of Delaware, N00014-05-1-0094 and N00014-05-1-0095 to RSMAS. The authors would like to thank Kevin Williams and Manny Fiedeiro for supporting this effort, and two anonymous reviewers for their constructive comments that helped significantly improve the manuscript.

Appendix A. Lagrangian variational analysis (LAVA) method

Drifter data positions $\mathbf{r}_{obs}$ and model velocity fields $\mathbf{u}_{mod}$ are blended together to reconstruct two-dimensional flows. The purpose of the methodology is to correct circulation structures whose size and dynamics can be well represented by the model but may appear shifted in space and time relative to observations due to inaccuracies in model initialization and/or forcing. The circulation

structures to be corrected are characterized a priori to have a length scale R, a time scale T, and a Lagrangian time scale T_L.

Considering such scaling (R,T,T_L) constant over a well-defined domain (shelf or offshore), the reconstruction consists of computing time-independent sequential velocity corrections $\Delta\mathbf{u}(t_o)$ for successive sampling sequences $[t_o, t_o+\tau]$ in the neighborhood of drifter trajectories. The sequence duration τ is chosen to be approximately T_L for a consistent sampling of the corrected structures. The time-dependent velocity field is then reconstructed as

$$\mathbf{u}_e(t) = \mathbf{u}_{mod}(t) + \Delta\mathbf{u}(t_o) \quad \text{for } t \in [t_o - \tau/2, t_o + \tau/2]. \tag{A.1}$$

For each sequence $[t_o, t_o+\tau]$, an inverse problem is solved. The velocity correction $\Delta\mathbf{u}$ minimizes the misfit between trajectories simulated using $\mathbf{u}_{mod}$ and observed positions $\mathbf{r}_{obs}$ (Taillandier et al., 2006a). This minimization problem is solved using a variational approach formulated as follows:

Stage 1: The position $\mathbf{r}_{\mathbf{obs}}(t_o+\tau)$ is predicted from a trajectory simulation solving the nonlinear differential equation

$$d_t\mathbf{r} = \mathbf{u}_{mod}(\mathbf{r}(t),t) \quad \text{for} \quad t \in [t_o, t_o+\tau], \quad \text{with } \mathbf{r}(t_o) = \mathbf{r}_{obs}(t_o), \tag{A.2}$$

where d_t is the first order derivative in time. This position prediction can be written as $\mathbf{r}(t_o+\tau) = \mathbf{H}_{NL}(\mathbf{u}_{mod})$ for the nonlinear operator $\mathbf{H}_{NL}$. The distance between observed and simulated positions is then expressed by the cost function

$$J = \frac{1}{2}(\mathbf{r}_{obs}(t_o+\tau) \cdots - \mathbf{H}_{NL}(\mathbf{u}_{mod}))^T(\mathbf{r}_{obs}(t_o+\tau) - \mathbf{H}_{NL}(\mathbf{u}_{mod})), \tag{A.3}$$

where ^{T} denotes the vector transpose. Components of the position difference are assumed to be independent. They are associated with Gaussian homogeneous errors, so that the observational error covariance matrix, used for the scalar product in Eq. (A.3), is the identity matrix.

Stage 2: The optimal velocity correction $\Delta\mathbf{u}$ is estimated by minimizing J using a steepest descent procedure, along the gradient

$$\nabla J = -\mathbf{B}\mathbf{H}^T(\mathbf{r}_{obs}(t_o+\tau) - \mathbf{H}_{NL}(\mathbf{u}_{mod})), \tag{A.4}$$

where $\mathbf{B}$ is the background error covariance matrix, $\mathbf{H}$ the tangent linear operator associated with $\mathbf{H}_{NL}(\mathbf{u}_{mod})$, and $\mathbf{H}^T$ its adjoint operator. $\mathbf{B}$ is built by finite iterations of the diffusion equation (Derber and Rosati, 1989; Weaver and Courtier, 2001) in order to spread each along-trajectory velocity correction throughout its neighborhood. Note that the number of iterations depends on the characteristic length scale R. $\mathbf{H}$ is defined by the perturbation equation associated with Eq. (A.2), as explicitly derived in a discrete formalism by Taillandier et al. (2006a).

Appendix B. Normal mode analysis (NMA) method

The description here follows Lipphardt et al. (2000). A more detailed derivation can be found in Eremeev et al. (1992a,b) and Chu et al. (2003).

The three-dimensional incompressible velocity field is expressed in terms of two scalar potentials as

$$\mathbf{u} = \nabla \times \left[\hat{\mathbf{k}}(-\Psi) + \nabla \times \left(\hat{\mathbf{k}}\Phi\right)\right], \tag{B.1}$$

where $\hat{\mathbf{k}}$ is the unit vector in the vertical direction. Note that this form ensures that the velocity field is exactly incompressible in three dimensions.

Calculation of the vertical component of relative vorticity from Eq. (B.1) in a Cartesian coordinate system leads to a Helmholtz equation for Ψ. Here, Ψ is represented as a set of eigenfunctions, which we call Dirichlet modes (ψ_n). The ψ_n, which may be thought of as streamfunction or vorticity modes with zero horizontal divergence, are solutions to

$$\nabla^2\psi_n + \lambda_n\psi_n = 0, \quad \psi_n|_{\partial D} = 0, \tag{B.2}$$

where D denotes the domain and ∂D its boundary.

Calculation of the vertical velocity component from Eq. (B.1) in a Cartesian coordinate system leads to a Helmholtz equation for $\widetilde{\Phi} \equiv \partial\Phi/\partial z$. We represent $\widetilde{\Phi}$ as a set of eigenfunctions, which we call Neumann modes (ϕ_m). The ϕ_m, which may be thought of as velocity potential or divergence modes with zero relative vorticity, are solutions to

$$\nabla^2\phi_m + \mu_m\phi_m = 0, \quad (\hat{\mathbf{n}} \cdot \nabla\phi_m)|_{\partial D} = 0, \tag{B.3}$$

where $\hat{\mathbf{n}}$ is the unit outward normal vector on the boundary.

From Eq. (B.1) and restricting out attention to the horizontal velocities, the gradients of ψ_n and ϕ_m can be expressed as

$$\mathbf{u}_n^D = \left(\frac{-\partial\psi_n}{\partial y}, \frac{\partial\psi_n}{\partial x}\right), \tag{B.4}$$

$$\mathbf{u}_m^N = \left(\frac{\partial\phi_m}{\partial x}, \frac{\partial\phi_m}{\partial y}\right). \tag{B.5}$$

The analysis domain used here is rectangular, so that the ψ_n and ϕ_m and their gradients are known analytically. Both eigenfunction sets are ordered by decreasing spatial scale, with the first mode having the largest spatial scale. Note that both the ψ_n and ϕ_m result in no normal flow on the domain boundary. Since our analysis domain is in the open ocean, flow across the domain boundary is anticipated. To account for the normal component of the flow at the domain's open boundaries, a boundary velocity potential solution Θ is calculated numerically (using a Matlab implementation of the generalized minimum residual method) as the solution to

$$\nabla^2\Theta = S_\Theta, \quad (\hat{\mathbf{n}} \cdot \nabla\Theta)|_{\partial D} = (\hat{\mathbf{n}} \cdot \mathbf{u}_{mod})|_{\partial D}, \tag{B.6}$$

where $\mathbf{u}_{mod}$ are model velocities and S_Θ is a source term that accounts for the net flow into the domain through its open boundaries, defined as

$$S_\Theta = \frac{\oint_{\partial D} \hat{\mathbf{n}} \cdot \mathbf{u}_{mod} dl}{\int\int_D dx\,dy}. \tag{B.7}$$

From Θ, boundary solution velocities are computed as

$$\mathbf{u}_{bdry} = \nabla\Theta(x,y). \tag{B.8}$$

For convenience, we will refer to a single set of basis functions $\mathbf{u}_k$ that includes both the $\mathbf{u}_n^D$ and $\mathbf{u}_m^N$. With this notation, the complete estimated velocity field at a given depth is given by

$$\mathbf{u}_e(x,y,t) = \mathbf{u}_{bdry}(x,y,t) + \sum_{k=1}^{K} a_k(t)\mathbf{u}_k(x,y). \tag{B.9}$$

At each time t, the amplitudes $a_k(t)$ are solutions to the minimization problem

$$\min_{\mathbf{a}} \|\mathbf{A}\mathbf{a} - \mathbf{b}\|_2, \tag{B.10}$$

where

$$\mathbf{a} = \begin{bmatrix} a_1(t) \\ a_2(t) \\ \vdots \\ a_K(t) \end{bmatrix},$$

$$\mathbf{A} = \begin{bmatrix} \mathbf{u}_1(\mathbf{x}_1) & \cdots & \mathbf{u}_K(\mathbf{x}_1) \\ \mathbf{u}_1(\mathbf{x}_2) & \cdots & \mathbf{u}_K(\mathbf{x}_2) \\ \vdots & \cdots & \vdots \\ \mathbf{u}_1(\mathbf{x}_{N_{grid}}) & \cdots & \mathbf{u}_K(\mathbf{x}_{N_{grid}}) \end{bmatrix}, \tag{B.11}$$

$$\mathbf{b} = \begin{bmatrix} \mathbf{u}_{mod}(\mathbf{x}_1, t) - \mathbf{u}_{bdry}(\mathbf{x}_1, t) \\ \mathbf{u}_{mod}(\mathbf{x}_2, t) - \mathbf{u}_{bdry}(\mathbf{x}_2, t) \\ \vdots \\ \mathbf{u}_{mod}(\mathbf{x}_{N_{grid}}, t) - \mathbf{u}_{bdry}(\mathbf{x}_{N_{grid}}, t) \end{bmatrix}.$$

The system is overdetermined for $N_{grid} > K$, and the a_k are determined through least squares minimization. If $N_{grid} = K$, then $\mathbf{Aa} = \mathbf{b}$ can be solved, reproducing the model velocities exactly on the grid. When $N_{grid} < K$, the underdetermined system may be solved in a minimum norm sense. The last two cases do not occur in this study.

When drifter velocities are also available, they might simply be added as additional elements in $\mathbf{b}$ above. For the NMA mappings used here, however, there are typically thousands of model velocities and no more than 30 drifter velocities. In this case, treating drifter velocities the same as model velocities gives the drifter observations very little weight.

Since we anticipate differences between model and drifter velocities and we desire to use the drifters to correct the model forecasts, the drifter velocities are used as a separate constraint on the least-squares minimization problem (B.10) (Toner et al., 2001). Drifter paths $\mathbf{r}_p(t)$ $(p = 1,\ldots,N_{drift})$ and the associated velocities $\boldsymbol{\mu}_p(t)$ $(p = 1,\ldots,N_{drift})$, computed from Hermite cubic interpolations of the positions along these paths, provide this additional constraint:

$$\mathbf{Ba} = \mathbf{d}, \tag{B.12}$$

where

$$\mathbf{B} = \begin{bmatrix} \mathbf{u}_1(\mathbf{r}_1(t)) & \cdots & \mathbf{u}_K(\mathbf{r}_1(t)) \\ \mathbf{u}_1(\mathbf{r}_2(t)) & \cdots & \mathbf{u}_K(\mathbf{r}_2(t)) \\ \vdots & \cdots & \vdots \\ \mathbf{u}_1\left(\mathbf{r}_{N_{drift}}(t)\right) & \cdots & \mathbf{u}_K\left(\mathbf{r}_{N_{drift}}(t)\right) \end{bmatrix},$$

$$\mathbf{d} = \begin{bmatrix} \boldsymbol{\mu}_1(\mathbf{r}_1(t)) - \mathbf{u}_{bdry}(\mathbf{r}_1(t)) \\ \boldsymbol{\mu}_2(\mathbf{r}_2(t)) - \mathbf{u}_{bdry}(\mathbf{r}_2(t)) \\ \vdots \\ \boldsymbol{\mu}_{N_{drift}}\left(\mathbf{r}_{N_{drift}}(t)\right) - \mathbf{u}_{bdry}\left(\mathbf{r}_{N_{drift}}(t)\right) \end{bmatrix}. \tag{B.13}$$

In the case at hand, the domain is a rectangle, leading to analytic basis functions $\mathbf{u}_k$, which are evaluated directly to generate velocities at drifter locations $\mathbf{u}_k(\mathbf{r}_p(t))$. The numerical boundary solution $\mathbf{u}_{bdry}$ is bilinearly interpolated to the drifter locations.

The least squares problem (B.10) subject to the constraint (B.12) has a unique solution when $\mathbf{B}$ has full row rank and

$$\begin{bmatrix} \mathbf{A} \\ \mathbf{B} \end{bmatrix} \tag{B.14}$$

has full column rank, as is always the case here. We solve this system using a Matlab implementation of the QR factorization technique.

Appendix C. Sonobuoy field drift model (SFDM)

SFDM is a collection of Matlab routines and a Fortran module that calculate sonobuoy trajectories from their initial positions and hydromechanical properties, using a model velocity field. Based on the initial conditions, a velocity vertical profile is developed for each buoy by three-dimensional linear interpolation of the u and v model velocity components. These profiles are passed to the sonobuoy drift response model to derive the drift velocity, which is in turn used to update the sonobuoy position for the next time step with a simple forward Euler step. The code can be found in Hammond (2005).

The drift response model is a modified version of the Navy standard sonobuoy model FF2E, described by Wang and Moran (1980). FF2E is a two-dimensional steady state cable model that is used as a standard design and evaluation tool in the commercial sonobuoy industry. It predicts the steady state response (including drift velocity) of a free-floating cable-body system to a two-dimensional current profile. It has been extensively tested and validated (e.g., McEachern, 1980). Wind drag is incorporated into FF2E, but was not used in the present application (see Section 4).

Real world current fields typically have a complex three-dimensional structure. FF2E, however, is restricted to two dimensions, and the sonobuoy response is calculated separately for two orthogonal horizontal velocity components. To minimize the resulting drift error of up to nearly 30% (Hammond, 2005), these components do not necessarily coincide with u and v but rather are rotated for one of them to align with the predominant current direction, determined by a weighted mean. The rotation angle α is given by

$$\alpha = \sum_z \arctan\left(\frac{v(z)}{u(z)}\right) \frac{u^2(z) + v^2(z)}{\sum_z (u^2(z) + v^2(z))}. \tag{C.1}$$

FF2E considers a free-floating system consisting of a surface buoy, an arbitrary number of cable segments and intermediate bodies, and a terminal weight at the bottom. The ingested velocity profile is assumed to be a function of depth alone. At equilibrium, the entire system will drift at a velocity u_D and the surface buoy will have a draft depth H. These two variables are determined iteratively. For each iteration, the current values for u_D and H are used to derive the tension and angle on the cable just below the buoy. The equilibrium equations are then integrated down the cable, accounting for the intermediate bodies along the way. Equilibrium is checked at the bottom unit:

$$e_H = T_H - D_B, \tag{C.2}$$

$$e_V = T_V - W_B, \tag{C.3}$$

where e_H and e_V are the horizontal and vertical imbalances, T_H and T_V are the horizontal and vertical components of the tension just above the bottom unit, and D_B and W_B are the drag and weight in water of the bottom unit. Various criteria on the imbalances can be imposed; here the iteration is stopped when both of the following inequalities are satisfied:

$$|e_H| < \epsilon_1 |D_B|, \tag{C.4}$$

$$|e_V| < \epsilon_2 |W_B| \tag{C.5}$$

for $\epsilon_{1,2}$ small positive constants (taken to be 0.02 here).

To start the iteration, H is a function of the buoyancy required to support the weight of the entire system in water in the absence of currents, while u_D is determined by a bisection scheme to reduce e_H alone. If at the end of this step e_V is still too large, a simultaneous scheme is used. If convergence fails under this scheme, a solution is found with a staggered scheme.

For the simultaneous scheme, u_D and H are updated using

$$\Delta u_D = \frac{\delta\delta_H |e_H| e_H}{EM_u} \quad \text{and} \tag{C.6}$$

$$\Delta H = \frac{-\delta |e_V| e_V}{EM_v}, \tag{C.7}$$

where $E = \sqrt{e_H^2 + e_V^2}$ is the combined equilibrium error, M_u and M_v are numerical factors defined below, and δ and δ_H are positive proportionality quantities chosen to facilitate convergence. The numerical factors are given by

$$M_u = \rho C_D A_T \frac{\Delta c}{2}, \tag{C.8}$$

$$M_v = \rho g \pi \frac{d_S}{4}, \tag{C.9}$$

with ρ the fluid density, Δc the difference between maximum and minimum current, g the gravitational constant, d_S the diameter of the surface buoy, and $C_D A_T$ defined by

$$C_D A_T = \left(C_D A_S + \sum_{k=1}^{K} C_{Dk} l_{ok} d_{ok} + \sum_{k=1}^{K} C_D A_{lk} \right). \tag{C.10}$$

For the above equation the following definitions were used: $C_D A_S$ is the drag area of the surface buoy. K is the total number of cable segments. C_{Dk}, l_{ok}, d_{ok} are the drag coefficient, reference length, and reference diameter of the kth cable segment, respectively. $C_D A_{lk}$ is the drag area of the kth body.

The two proportionality quantities are initialized as 1. If e_H changes too fast (slow), δ_H is increased (decreased). If the updated values for H and u_D lead to an increased error E, Δu_D and ΔH are recalculated with the previous values and a reduces value for δ. δ is continually reduced until one of the following three conditions holds (where updated quantities are represented with a prime):

1. $E' < E$,
2. $e'_H / e_H > I$ and $|e'_H| > |e'_V|$, where I is the drag force per unit length normal to the cable,
3. δ is less than a prescribed lower bound (0.2 for the first ten iterations, 0.05 thereafter).

In any of these cases, δ is reset to 1.

If the simultaneous scheme as described above does not converge, a staggered scheme is used. This scheme searches for appropriate values for u_D and H successively. u_D is updated using a bisection method, with the sign of Δu_D determined by Eq. (C.6). H is updated using

$$\Delta H = \frac{-\delta_V e_V}{M_v}. \tag{C.11}$$

The proportionality quantity δ_V is initially set to 0.6 and adjusted if convergence is too slow or changes in H are too large.

Details of the drag calculations can be found in McEachern (1980).

References

Apte, A., Jones, C.K.R.T., Stuart, A.M., 2008. A Bayesian approach to Lagrangian data assimilation. Tellus A 60 (2), 336–347.

Aref, H., 1984. Stirring by chaotic advection. J. Fluid Mech. 143, 1–21.

Bauer, S., Swenson, M.S., Griffa, A., 2002. Eddy mean flow decomposition and eddy diffusivity estimates in the tropical Pacific Ocean: 2. Results. J. Geophys. Res. 107 (C10), 3154.

Chu, P.C., Ivanov, L.M., Korzhova, T.P., Margolina, T.M., Melnichenko, O.V., 2003. Analysis of sparse and noisy ocean current data using flow decomposition. Part i: Theory. J. Atmos. Ocean. Technol. 20 (4), 478–491.

Coughlan, R., 1975. Effects of wind and water drag on sonobuoy surface floats. Technical Report, 2063-TM-31-75, NAVAIRDEVCEN.

Derber, J., Rosati, A., 1989. A global oceanic data assimilation system. J. Phys. Oceanogr. 19 (9), 1333–1347.

Eremeev, V.N., Ivanov, L.M., Kirwan, A.D., 1992a. Reconstruction of oceanic flow characteristics from quasi-Lagrangian data. 1: Approach and mathematical methods. J. Geophys. Res. 97 (C6), 9733–9742.

Eremeev, V.N., Ivanov, L.M., Kirwan, A.D., Melinchenko, O.V., Kochergin, S.V., Stanichaya, R.R., 1992b. Reconstruction of oceanic flow characteristics from quasi-Lagrangian data. 2: Characteristics of the large-scale circulation in the Black Sea. J. Geophys. Res. 97 (C6), 9743–9753.

Fox, D.N., Teague, W.J., Barron, C.N., Carnes, M.R., Lee, C.M., 2002. The modular ocean data assimilation system (MODAS). J. Atmos. Oceanic Technol. 19 (2), 240–252.

Griffa, A., Piterbarg, L.I., Özgökmen, T., 2004. Predictability of Lagrangian particle trajectories: Effects of smoothing of the underlying Eulerian flow. J. Mar. Res. 62 (1), 1–35.

Hammond, D.S., 2005. Sonobuoy field drift prediction. Technical Report, Naval Air Warfare Center Aircraft Division, Department of the Navy. <http://handle.dtic.mil/100.2/ADA430511>.

Hammond, D.S., 2008a. Optimal deployment of drifting acoustic sensors. Technical Report, Advanced Avionics, Inc.

Hammond, D.S., 2008b. Sonobuoy drift simulation: LWAD 07-2. Technical Report, Advanced Avionics, Inc.

Hernandez, F., LeTraon, P.Y., Morrow, R., 1995. Mapping mesoscale variability of the Azores Current using TOPEX/POSEIDON and ERS 1 altimetry, together with hydrographic and Lagrangian measurements. J. Geophys. Res. 100 (C12), 24995–25006.

Ide, K., Kuznetsov, L., Jones, C.K.R.T., 2002. Lagrangian data assimilation for point vortex systems. J. Turbul. 3, 053.

Kamachi, M., O'Brien, J.J., 1995. Continuous data assimilation of drifting buoy trajectory into an equatorial Pacific Ocean model. J. Marine Syst. 6 (1–2), 159–178.

Krause, P., Restrepo, J.M., 2009. The diffusion kernel filter applied to Lagrangian data assimilation. Mon. Weather Rev. 137 (12), 4386–4400.

Kuznetsov, L., Ide, K., Jones, C.K.R.T., 2003. A method for assimilation of Lagrangian data. Mon. Weather Rev. 131 (10), 2247–2260.

LaCasce, J.H., 2008. Statistics from Lagrangian observations. Prog. Oceanogr. 77 (1), 1–29.

Lipphardt, B.L., Kirwan, A.D., Grosch, C.E., Lewis, J.K., Paduan, J.D., 2000. Blending HF radar and model velocities in Monterey Bay through normal mode analysis. J. Geophys. Res. 105 (C2), 3425–3450.

Martin, P.J., 2000. Description of the Navy Coastal Ocean Model Version 1.0. Technical Report, Ocean Dynamics and Prediction Branch, Oceanography Division, NRL.

McEachern, J.F., 1980. A modification to the free floating extensible cable system computer model (ff2e) to consider lift and drag forces on intermediate bodies. Technical Report, Naval Air Development Center. <http://handle.dtic.mil/100.2/ADA092512>.

Molcard, A., Piterbarg, L., Griffa, A., Özgökmen, T.M., Mariano, A.J., 2003. Assimilation of drifter observations for the reconstruction of the Eulerian circulation field. J. Geophys. Res. 108 (C3), 3056.

Molcard, A., Griffa, A., Özgökmen, T.M., 2005. Lagrangian data assimilation in multilayer primitive equation ocean models. J. Atmos. Oceanic Technol. 22 (1), 70–83.

Nodet, M., 2006. Variational assimilation of Lagrangian data in oceanography. Inverse Prob. 22 (1), 245–263.

Özgökmen, T.M., Molcard, A., Chin, T.M., Piterbarg, L.I., Griffa, A., 2003. Assimilation of drifter observations in primitive equation models of midlatitude ocean circulation. J. Geophys. Res. 108 (C7), 3238.

Rao, D.B., Schwab, D.J., 1981. A method of objective analysis for currents in a lake with application to Lake Ontario. J. Phys. Oceanogr. 11 (5), 739–750.

Riedlinger, S., Preller, R., Martin, P., 2006. Validation Test Report for the 1/16°East Asian Seas Navy Coastal Ocean Model Nowcast/Forecast System. Technical Report, Ocean Dynamics and Prediction Branch, Oceanography Division, NRL.

Salman, H., 2008a. A hybrid grid/particle filter for lagrangian data assimilation. i: Formulating the passive scalar approximation. Q. J. R. Meteorol. Soc. 134 (635), 1539–1550.

Salman, H., 2008b. A hybrid grid/particle filter for Lagrangian data assimilation. ii: Application to a model vortex flow. Q. J. R. Meteorol. Soc. 134 (635), 1551–1565.

Salman, H., Kuznetsov, L., Jones, C.K.R.T., Ide, K., 2006. A method for assimilating Lagrangian data into a shallow-water-equation ocean model. Mon. Weather Rev. 134 (4), 1081–1101.

Taillandier, V., Griffa, A., 2006. Implementation of position assimilation for ARGO floats in a realistic Mediterranean Sea OPA model and twin experiment testing. Ocean Sci. 2 (2), 223–236.

Taillandier, V., Griffa, A., Molcard, A., 2006a. A variational approach for the reconstruction of regional scale Eulerian velocity fields from Lagrangian data. Ocean Modell. 13 (1), 1–24.

Taillandier, V., Griffa, A., Poulain, P.M., Béranger, K., 2006b. Assimilation of Argo float positions in the north western Mediterranean Sea and impact on ocean circulation simulations. Geophys. Res. Lett. 33 (11), L11604.

Taillandier, V., Griffa, A., Poulain, P.M., Signell, R., Chiggiato, J., Carniel, S., 2008. Variational analysis of drifter positions and model outputs for the reconstruction of surface currents in the central Adriatic during fall 2002. J. Geophys. Res. 113 (C4), C04004.

Taillandier, V., Dobricic, S., Testor, P., Pinardi, N., Griffa, A., Mortier, L., Gasparini, G.P., 2010. Integration of Argo trajectories in the Mediterranean Forecasting System and impact on the regional analysis of the western Mediterranean circulation. J. Geophys. Res. 115 (C3), C03007.

Toner, M., Kirwan, A.D., Kantha, L.H., Choi, J.K., 2001. Can general circulation models be assessed and their output enhanced with drifter data? J. Geophys. Res. 106 (5), 19563–19579.

Wang, H.T., Moran, T.L., 1980. Analysis of the two-dimensional steady-state behavior of extensible free-floating cable systems. Technical Report, Naval Ship Research and Development Center. <http://handle.dtic.mil/100.2/AD738000>.

Weaver, A., Courtier, P., 2001. Correlation modelling on the sphere using a generalized diffusion equation. Q.J. R. Meteorol. Soc. 127 (575), 1815–1846.